REPUBLIC OF TURKEY
YILDIZ TECHNICAL UNIVERSITY
GRADUATE SCHOOL OF NATURAL AND APPLIED SCIENCES

FABRICATION, PROPERTIES AND INVESTIGATION OF THE STRENGTH BEHAVIOUR OF BULK WC-12Co HARD MATERIALS CONSOLIDATED BY SPARK PLASMA SINTERING

ALİHAN AYGÜN

MSc. THESIS
DEPARTMENT OF METALLURGICAL AND MATERIALS ENGINEERING
PROGRAM OF MATERIALS ENGINEERING

ADVISER
PROF. DR. AHMET TOPUZ

ISTANBUL, 2013

REPUBLIC OF TURKEY
YILDIZ TECHNICAL UNIVERSITY
GRADUATE SCHOOL OF NATURAL AND APPLIED SCIENCES

FABRICATION, PROPERTIES AND INVESTIGATION OF THE STRENGTH BEHAVIOUR OF BULK WC-12Co HARD MATERIALS CONSOLIDATED BY SPARK PLASMA SINTERING

A thesis submitted by Alihan AYGÜN in partial fulfillment of the requirements for the degree of **MASTER OF SCIENCE** is approved by the committee on 07.01.2014 in Department of Metalurgical and Materials Engineering Department, Materials Engineering Program.

Thesis Adviser
Prof. Dr. Ahmet TOPUZ
Yildiz Technical University

Approved By the Examining Committee
Prof. Dr. Ahmet TOPUZ
Yildiz Technical University ______________________

Prof. Dr. Müzeyyen MARŞOĞLU, Member
Yildiz Technical University ______________________

Prof. Dr. Ayşegül AKDOĞAN EKER, Member
Yildiz Technical University ______________________

ACKNOWLEDGEMENTS

This thesis has been done in TU BA Freiberg with collaboration Yildiz Technical University during my erasmus programme.

I would like to express my appreciation to my advisory committee: Prof. Dr.-Ing. L. Krüger, Prof. Dr. A. Topuz, Dipl. Ing. K. Mandel. Thanks for giving me the opportunity to be part of the WC-Co hard metal research. They have shown in me, valuable scientific suggestions, good guidance and for reviewing and improving my reports. Also, thanks to the TU BA Freiberg for making this study possible.

Dipl.-Ing. K. Mandel, I owe you so much. You’ve been, my mentor, my colleague, my friend and a never-ending fount of moral support. You have given so much of yourself to help me succeed.

I would also like to thank Dipl.-Ing. M. Radajewski for helping my first experimentals of this project.

Finally, I would like to dedicate this work to my family. Without your unending support and love from childhood to now, I never would have made it through this process or any of the tough times in my life. Thank you.

January, 2014

Alihan AYGÜN

TABLE OF CONTENTS

CHAPTER 1

CHAPTER 2

CHAPTER 3

CHAPTER 4

CHAPTER 5

LIST OF SYMBOLS

A_F	Amplification factor
Å	Angstrom ($1x10^{-10}$ m)
β	Binder phase
C	BET constant
C_{WC}	Contiguity of WC phase
d_o	Diameter of sample (mm)
d_1, d_2	Diagonal of the hardness indentation
D	Roughness factor at BET analysis
d_i,d_a	Inner and outer diameter (mm)
$\bar{d}_{Par}$	Mean grain size (nm)
d_{WC}	WC grain size (nm)
E	Elastic Modulus (GPa)
ε	Strain
$\dot{\varepsilon}$	Strain rate (s^{-1})
F	Force (N)
F_{max}	Maximum force (N)
h_o	Height of sample (mm)
H	Hardness
HV30	Vickers hardness (F=294,2 N)
K_{Ic}	Fracture toughness ($MPa\sqrt{m}$)
λ_{Co}	The mean free path of Co phase (nm)
L_i	Total length of the each cut area (WC or Co)
m_a	Specific adsorbed mass
m_1	Mass of dry sample (g)
m_2	Mass of sample in water (g)
m_{HM}	Mass of WC-Co hard metal (g)
M_s	Martensitic transformation
η	Eta phase
n_a	Specific adsorbed amount (mol/g)
n_m	Monolayer capacity of adsorbate (mol/g)
N_i	Number of the areas due to the line intercept method (WC or Co)
υ	Poisson’s Ratio
P_{el}	Electrical power (kW)
p_o	Saturation vapor pressure of the adsorptive (Pa)
p/p_o	Relative pressure
R_i	Single crack resistance (J)
R_p	Yield strength (MPa)
ρ_i	Density (g/cm^3)
ρ_{rel}	Relative denstiy (g/cm^3)

ρ_{th}	Theoretical density (g/cm^3)
S_o	Cross sectional area (mm^2)
S_{BET}	Specific surface area (m^2/g)
Σl_i	Sum of the crack length (µm)
σ_{CS}	Compressive strength (MPa)
$\dot{T}_{Cool}$	Cooling rate (K/min)
$T_{Melting}$	Melting temperature (^oC)
T_{Sinter}	Sintering temperature (^oC)
t_{Sinter}	Sintering time (min)
$t_{milling}$	Milling time (min)
V_{Co}	Volume fraction of Co phase (%)
V_g	Bridge voltage (V)
V_{Por}	Volume fraction of pores (%)
V_s	Supply voltage (V)
V_{WC}	Volume fraction of WC phase (%)
v_1	Longitudinal sound wave speed (m/s)
v_{Piston}	Piston speed (m/s)
v_t	Transversal sound wave speed (m/s)
x_i	Mass fraction (%)
Z	Atomic number

LIST OF ABBREVIATIONS

AC	Alternating Current
BPR	Ball Powder Ratio
BSE	Backscattered Electrons
DC	Direct Current
FAST	Field Assisted Sintering Technology
fcc	face centered cubic
hcp	hexogonal close packed
HIP	Hot Isostatic Pressing
HP	Hot Pressing
HR	Heat Rate
PAS	Plasma Assisted Sintering
PCAS	Pulsed Current Activated Sintering
PECS	Pulsed Electric Current Sintering
PPS	Pulse Plasma Sintering
SE	Secondary Electrons
SEM	Scanning Electron Microscopy
SHPB	Split Hopkinson Pressure Bar (Test)
SPS	Spark Plasma Sintering
TRS	Transverse Rupture Strength

LIST OF FIGURES

Page

LIST OF TABLES

ABSTRACT

FABRICATION, PROPERTIES AND INVESTIGATION OF THE STRENGTH BEHAVIOUR OF BULK WC-12Co HARD MATERIALS CONSOLIDATED BY SPARK PLASMA SINTERING

Alihan AYGÜN

Department of Metallurgical and Materials Engineering

MSc. Thesis

Adviser: Prof. Dr. Ahmet TOPUZ

WC–Co cemented carbides own attractive mechanical properties such as high hardness, wear/abrasion resistance and elastic modulus, as well as a good fracture toughness, which make them extensively used in several areas, in particular, as cutting and machining tools. Hence, owing to their practical importance, several studies have been carried out in the last decades to investigate and improve their mechanical properties.

The mechanical properties of SPS sintered compact show different characteristics compared to conventional pressure assisted sintering processes. The advantage and characteristics of this process are the easy controllability of the parameters to control the microstructure, limit particle growth, capability to process the sinter retardant materials, and the reaction preventing effect between additives and base materials.

A literature review and experimental investigation were realised in this study. The literature review includes influence of milling and sintering parameters on the densification behaviour and the microstructure as well as the mechanical properties of WC-Co cemented carbides during sintering and the loading rate on the compressive strength of brittle materials. The experimental study consists of impression of the milling time on the powder characteristics and the densification, Co distribution of self-mixed WC-12Co and related mechanical and microstructure properties (indentation fracture mechanics, SEM-investigation) and measurement of the compressive fracture strength of WC-Co as a function of the loading rate.

Key words: Hard materials, spark plasma sintering, milling, compressive strength

---

ÖZET

SPARK PLAZMA SİNTERLEME TEKNİĞİYLE WC-12Co SERT METALİNİN ÜRETİLMESİ, ÖZELLİKLERİ VE DAYANIM DAVRANIŞININ ARAŞTIRILMASI

Alihan AYGÜN

Metalurji ve Malzeme Mühendisliği Anabilim Dalı
Yüksek Lisans Tezi

Tez Danışmanı: Prof. Dr. Ahmet TOPUZ

WC-Co kaynaşık karbürleri yüksek sertlik, aşınma dayanımı ve elastik modüllerinin yanı sıra yüksek kırılma tokluğu gibi etkileyici özelliklere sahiptir. Bu özellikleri onları kesme ve talaşlı imalat gibi birçok alanda yoğun şekilde kullanılır hale getirmiştir. Bu yüzden son birkaç on yıl içinde mekanik özelliklerinin araştırılması ve geliştirilmesi üzerine birçok çalışma yapılmıştır.

SPS yöntemiyle üretilmiş malzemelerin mekanik özellikleri geleneksel yöntemlerle sinterlenmiş olanlardan farklıdır. Mikroyapı özelliklerinin ve tane büyümesinin kontrol edilebilmesi, sinterlenmesi güç olan malzemelerin sinterlenebilmesi ve katkı malzemeleriyle ana bileşen arasındaki reaksiyonu önleyici etkisi bu yöntemin avantajları ve karakteristik özellikleridir.

Bu çalışmada literatur incelemesi ve deneysel araştırmalar gerçekleştirilmiştir. Literatür incelemesi, öğütme ve sinter parametrelerinin yoğunlaşma, mikro yapı, SPS yöntemiyle üretilmiş WC-12Co sert metalinin mekanik özellikleri üzerindeki etkilerini ve yükleme hızının kırılgan malzemelerin basma dayanımına olan etkisini içermektedir. Deneysel araştırmalar öğütme zamanın yoğunlaşma ve toz karakteristiği üzerindeki etkisinin araştırılmasına, WC-12Co sert metalinin ilgili mekaniksel ve mikroyapısal özelliklerinin (kırılma mekaniği, SEM araştırmaları) incelenmesine ve yükleme hızının bir fonksiyonu olarak basma dayanımının ölçülmesine yöneliktir.

Anahtar Kelimeler: Sert malzemeler, spark plazma sinterleme, öğütme, basma dayınımı

CHAPTER 1

INTRODUCTION

1.1 Literature Review

Cemented tungsten carbides are commercially one of the oldest and most successful powder metallurgy products. Cemented carbides is a class of materials with much industrial importance, and used for instance in metal working, mining, wear parts and other applications that require the combination of high hardness and reasonable toughness. In its simplest form the cemented carbide consists of WC as hard phase and Co as cementing binder phase [1].

1.2 Objective of the Thesis

Several studies have been carried out on various aspects involved in manufacturing of such ultrafine/nanograined cemented carbides and their superior mechanical properties such as high hardness, high temperature strength and elastic modulus. While these mechanical properties depend on many factors such as alloy composition, purity, homogeneity of the structure and particle size of the initial powder, for a given alloy composition it is the microstructure (WC grain size, mean free path of cobalt and the contiguity of WC particles) that decides the mechanical properties. The final microstructure depends on the type of sintering process adopted and the sintering parameters such as temperature, time, pressure and atmosphere.

1.3 Hypothesis

Sintering densification is another important procedure to achieve the dense hard alloys. There have been many sintering methods, such as vacuum sintering, hot pressing, hot isostatic pressing (HIP), pulsed current activated sintering (PCAS), microwave sintering, high-frequency induction sintering and the newly developed spark plasma sintering (SPS). It is well known that for the conventional methods, in order to get the high density of the sintered WC–Co bulk, a high sintering temperature and a long holding time are usually used. As a result, the WC grain size in the densified bulk is prone to increase into the scale of micrometer. Particularly, the new SPS technique enables the powder compact to be densified by Joules heating when the pulsed direct current goes through the powder sample. Owing to the features of rapid heating and cooling rates, short holding time and unique consolidation mechanisms of the SPS process, the powder sample can be densified at relatively lower temperatures than in the conventional methods for the equivalent density of the sintered bulk. Moreover, the grain growth during sintering can be effectively inhibited.

CHAPTER 2

GENERAL INFORMATION

Henri Moissan who was working on synthetic diamonds found Tungsten monocarbide (WC, knows as tungsten carbide) in 1893. According to his research, the hardness of WC is close to diamonds hardness. Because of the brittleness of WC, it was not very convenient for commercial use. Initially, researchers have concentrated on making its toughness better. Then, Karl Schröter contributed greatly to the improvement of cemented carbides. He used cobalt (Co) as a binder phase and improved a compacting and sintering process which has extensive usage to product WC-Co hard metals. Modulating of part or all of the WC with other carbides, like titanium carbide (TiC), tantalum carbide (TaC), and/or niobium carbide (NbC) were the subsequent research that including modifications of Schröter's process [1].

2.1 Phase Relationship in W-Co-C System

A close-packed hexagonal form, ε, which shows stable property at temperatures below nearly 400°C, and a face centred cubic form, α, which shows stable property at higher temperatures are the two kinds of allotropic modifications of cobalt (Figure 2.1). According to reports, it is not permanent situation that the behaviors of a reversal of the cubic to the hexagonal form at temperatures in the area of the magnetic transformation (1100–1150°C). It is possibly up to the existence of interstitial impurities. Purity and temperature change rate severely affects the temperature of the allotropic transformation. According to the investigations, the tranformation temperature is 421.5 or 417^{o}C for the highest purity material (approx. 99.998%) and slow temperature change rate. The changing of the free energy during the transformation is low, nearly 500 J/mol for $\varepsilon \rightarrow \alpha$ and nearly 360 J/mol for $\alpha \rightarrow \varepsilon$, and this accounts for the sluggishness of the change and its sensitivity to experimental conditions is related to the free energy change. The stability of the two allotropes is effected by the grain size and at normal temperatures, a finer grain size favouring the cubic form.

When a normal solid cobalt sustained hot or cold deformation and then annealed and slowly cooled to normal temperature, the structure is not thoroughly hexagonal. A presence of the metastable cubic phase is always available.

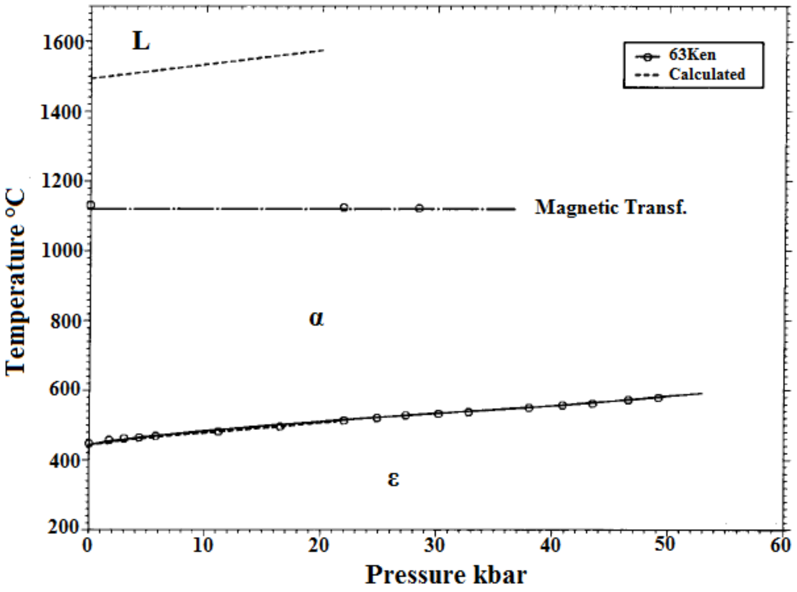

Figure 2.1 Assessed Co temperature-pressure phase diagram [2]

There are nearly identical quantities of the hexagonal and cubic phases in cobalt powder. In due course of milling, quantity of hexagonal cobalt rises to near 100 % and an annealing can not change cubic lattice of cobalt binder. The cause of this treatment are mechanical constraints that occur by stabilisation of the cubic modification by dissolved tungsten and carbon. The binder phase of a WC-Co cemented carbide was surveyed with chemical spectrometry by Gordon et al. It is affirmed that an ε-Co→α-Co allotropic transformation is near 727°C. At room temperature, mechanical strain can change it in the opposite direction. WC-Co cemented carbides with 8 %, 15 % and 20 % w/w of Co were studied by Yi and Jinghui. The transformation temperatures of hcp cobalt binder phase to fcc while heating were observed at 442 °C, 770 °C and 821 °C, respectively. The transformation temperature of cobalt phase is seriously up to the tungsten content. The transformation temperature increases with the increasing tungsten content in cobalt phase [3].

The most significant system for the production of cemented carbides is W-Co-C. A lot of effort was needed to determine the phase relations in this system thus far. Firstly, the approximation was just experimental. Then, it was combinated each other with thermodynamic calculations. Until now, there are differences betweeen the several phase diagrams. Also, there are some similarities.

- The phase WC, β (binder) and liquid are stable for compositions corresponding to a W/C atomic ratio close to one.

- A ternary brittle phase η occurs at lower carbon contents. Other ternary phases of W_2C would be stable only at a much lower carbon content or at a very low cobalt content, respectively.

- Primary carbon will precipitate and remain in equilibrium with WC and Co-rich- β phase in solidified alloys when the W/C atomic ratio is below 1.

- A narrow range of carbon concentration effects the presence of two phase WC-β.

In 1931, Wyman and Kelley have worked on the initial Co-WC diagram. In 1936, Takeda have done the first investigation of the W-Co-C phase system that is a tentative diagram including both stable and metastable equilibria. Rautala and Norton who have worked on the phase equilibria in the W-Co-C system through X-ray diffraction, metallographic and thermal analysis techniques offered temporary phase diagrams of stable, metastable equilibria and also two phases θ and κ, having compositions $Co_3W_6C_2$ and $Co_3W_{10}C_4$. The reactions which cause these phases were negotiated. In addition, a pseudobinary WC-Co diagram was recommended. Even if there were a relatively high carbon content following rapid cooling, the existence of η -phase in cemented carbides were not clarified with the diagram. Grüter, who clarified these suggestions that at temperatures from around 1280 to 1450°C, η-phase stays in equilibrium with WC and liquid even at stoichiometric compositions. Large η-phase zones can be retained there after solidification because of sintering of cemented carbides generally is seen in this temperature range. Güter achieved the pseudobinary WC-Co phase diagram that is indicated in Figure 2.2 [4].

2.1.1 Composition and microstructure of WC-Co hard metals

The non-centrosymmetric space group *P*-6*m*2 (No. 187) with one formula unit per unit cell which dimensions are a=2.906 Å and c=2.837 Å c/a=.976 causes crystallization of WC. The atoms are in the following special positions: W in 1 *a*: 0,0,0; C in 1 *d* : 1/3,2/3,1/2.

A projection through the *c* axis is seen in Figure 2.3. The atoms arrangement can be seen in close packed layers which are 36 nets composed of equilateral triangles of W and C in (0 0 0 1) planes. A, B, C and *α*, *β*, *γ* are stacking symbols. The Roman letters symbolize W atoms and the the Greek letters symbolize C atoms. It is related with the positions of the nodes of the nets of the hexagonal cell. A*γ* is the stacking repeat sequence for WC.

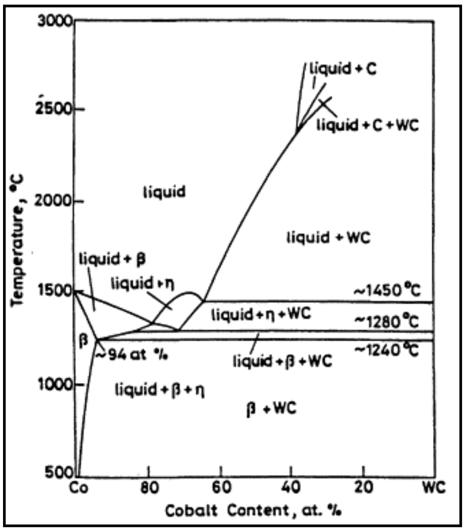

Figure 2.2 Vertical sections between stoichiometric WC and Co in W-Co-C phase diagram [4]

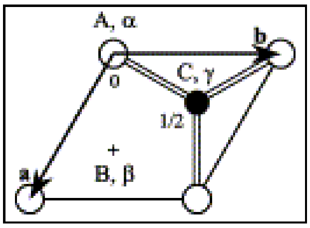

Figure 2.3 Unit cell of the WC structure projected along [0 0 0 1]. W, open circles; C, black circle. A, B, C and *α*,*β*,*γ* denote the stacking sites for close packed layers. Each atom in the WC structure is coordinated by six atoms of the other kind (indicated by three pairs of double lines) [5]

A trigonal prism (Fig. 2.4), W by six C at 2.197 Å, encircles all W atom in WC. Six W atoms coordinate every C atom because the structure is its own antistructure. The closest neighbor distance in pure tungsten, 2.735 Å can be compared with these distances [5].

The Cobalt content and WC grain size is useful for categorizing of WC-Co grades. Its name is "straight grades". The cemented carbide types which have perfect wear resistance show the large range of strength and toughness.

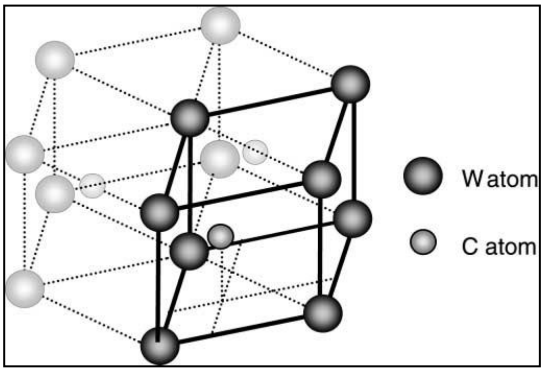

Figure 2.4 The atomic structure of WC crystal [6]

A classification of WC-Co hard metals in regard to grain size which is accepted all over the world was offered by the task-force `hard metals` of the German industrial union for powder metallurgy in 1999 (Table 2.1).

Table 2.1 Classification of hard metals due to grain size of the hard phase according to ISO 4499-2 [7]

Grain Size (µm)	**Name**
< 0.2	Nano
0.2-0.5	ultra fine
0.5-0.8	Submicron
0.8-1.3	Fine
1.3-2.5	Medium
2.5-6.0	Coarse
> 6.0	extra-coarse

Exceptional combinations of hardness and strength are obtainable on hard metals when the grain sizes are below 1 µm. The structure, i.e. the binder volume fraction V_{binder}, the contiguity of the WC phase C, the carbide grain size $d_{wc,}$ and the mean free path in the binder phase λ, identify the characteristics (Figure 2.5). The structure components can be determined by an examination of micrographs. The volume fractions of the carbide and binder phases are refered as composite composition. The recommended practice that is for prediction of the area fraction of a phase in a multiphase alloy by systematic point counting on a planary test section is obtained by ASTM. A prediction of the volume fraction, $(V_v)_\alpha$, area fraction, $(A_A)_\alpha$, and line fraction, $(L_L)_\alpha$ for random measurements is obtained by the point fraction, $(P_p)_\alpha$, that is intercepted by the α phase and statistically explicated [8].

$$(P_p)_\alpha=(L_L)_\alpha=(A_A)_\alpha=(V_v)_\alpha \tag{2.1}$$

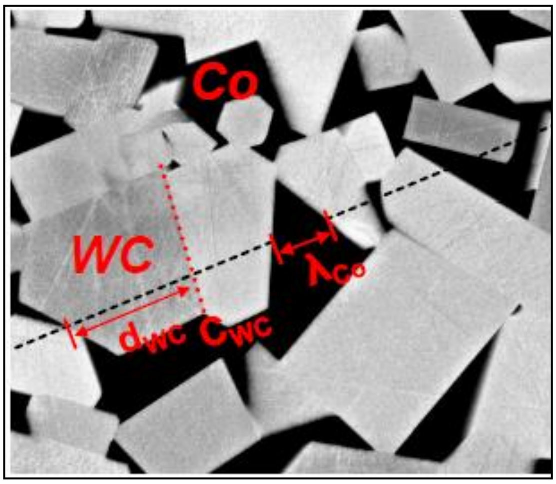

Figure 2.5 The microstructural paramaters in the WC-Co hard metal [9]

The boundary intercepts with test lines on planary sections provide the other structure parameters. The mean number of intercepts per unit length of test line with traces of the carbide/cobalt interface, $(N_L)_{WC/Co}$, and of carbide/carbide grain boundaries, $(N_L)_{WC/WC}$ should be indicated. So that, the mean carbide grain size can be established by these quantities.

$$d_{WC}=2(Vv)_{WC}/(2(N_L)_{WC/WC}+(N_L)_{WC/Co}) \tag{2.2}$$

the contiguity of the WC phase:

$$C=2(N_L)_{WC/WC}/(2(N_L)_{WC/WC}+(N_L)_{WC/Co}) \tag{2.3}$$

and the mean free path in the binder phase:

$$\lambda_m=2(V_V)_{binder}/(N_L)_{WC/C} \tag{2.4}$$

The value of V_{CO} can be calculated by equation 1.5 due to density of hard metal, Co and mass fraction of Co(%) [9].

$$V_{Co}=\frac{m_{Co}/\rho_{Co}}{m_{HM}/\rho_{HM}}=\frac{x_{Co}\cdot\rho_{HM}}{\rho_{Co}} \tag{2.5}$$

2.2 Spark Plasma Sintering

Production of nanostructured WC or WC-Co powders has been done with various technologies like the rapid carburization process, spraying conversion process, thermochemical precursor reduction, mechanochemical syntesis, high energy milling, etc.

The production of WC-Co has some unsolved processing problems. The treatment of agglomeration, larger interparticle friction, moisture absorption and higher oxidation rate is due to a higher specific area. Additionally, lower processing temperatures depend on higher sintering activity that is subject to reducing WC grain size. Grain growth results from fast sintering kinetics that is controlled difficulty.

Plasma Assisted Sintering (PAS), Pulsed Current Activated Sintering (PCAS), Pulse Plasma Sintering (PPS), Spark Plasma Sintering (SPS), etc. are the recent techniques for rapid sintering [10].

The latest trend, spark plasma sintering (SPS) is including one of the most important and efficient sintering techniques. SPS and hot pressing (HP) are nearly the same because of uniaxial pressure application across the sample while sintering process. SPS is more advantageous compare to HP, with HP materials may be sintered in hours but with SPS just in a matter of minutes. Concurrently, sintering tempratures are lower to determine full density. So that, the production of nanoscale structural material is possible. E.g. Tungsten carbide and hafnium diboride that are sintered diffuculty can be sintered easily via SPS technique without sintering agent. Uniaxial pressures (typically less than 100 MPa) and on-off dc pulsing current are used to sinter powders.

Figure 2.6 shows a basic diagram of the SPS apparatus. Several mechanisms are recommended for the improved sintering behaviour while on-off dc pulsing. Many of these mechanisms accept the existence of momently produced spark plasma among particles of powder.

A few of the SPS mechanisms situated in the literature are itemized below. According to the list, recommended SPS mechanisms are not overall.

1. spark impact pressure,
2. plasma cleaning of particle surfaces,
3. Joule’s rapid heating,
4. local melting and evaporation (especially in metallic systems),
5. surface activation on the particles,
6. electron wind force, and
7. field assisted diffusion

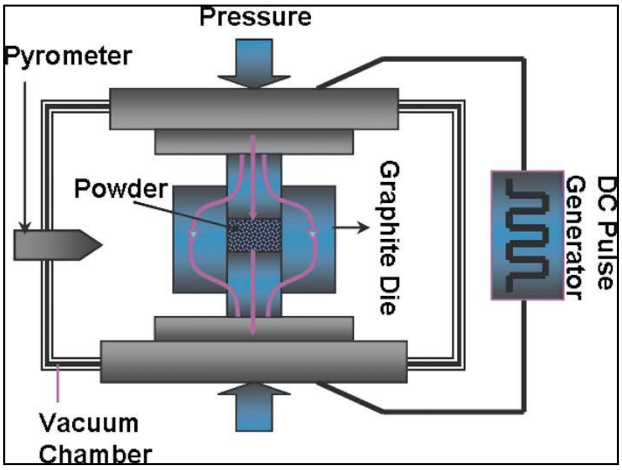

Figure 2.6 A schematic of the SPS process [11]

Joule's heating, local melting and evaporation (in metallic systems) have been comparatively well determined. The others, particularly apply the existence of plasma, are suppositional. SPS can be used to combine materials, grow crystals, advanced chemical reactions and production of materials which have different shapes without sintering [11].

SPS Syntex Inc. (Japan) and FCT SystemeGmbH (Germany) are two main producers for FAST (Field Assisted Sintering Technology)/SPS apparatus [12].

2.2.1 Powder Densification and Grain Growth

In a sintering system the reduction of interface energy of the system is the main driving force to sinter fine grained hard metals. This is achieved by reduction the area of the surfaces and interfaces of the compact, that occurs principally to combination of two simultaneous processes, nominately:

- *Densification* (displacement of the gas/solid interface by a lower-energy solid-solid or solid-liquid interface).
- *WC grain growth* (decrement of the solid-solid or solid-liquid interface area and occurence of low-energy prismatic interfaces) [13]

WC-Co cemented carbides include a great quantity of WC grains that are embedded in a binder phase (β). According to several sintering results, densification and grain growth take places in the solid state and are under the influence of the C content in (β) [14].

Densification means removing the porosity from a powder compact to produce a robust. (the theoretical density of a pore-free material is usually 95-98 %). Figure 2.7 shows a powder compact that illustrates two forms of porosity, inter and intraparticle. There is a common misapprehension that the crystal size of powder is tantamount to the actual size of the individual particle size. Principally, agglomerated larger particles nearly include individual crystallites. There are three mechanism (sintering, particle or crystal rearrangement and plastic deformation) to densification and during consolidation of a powder compact occurs one of them.

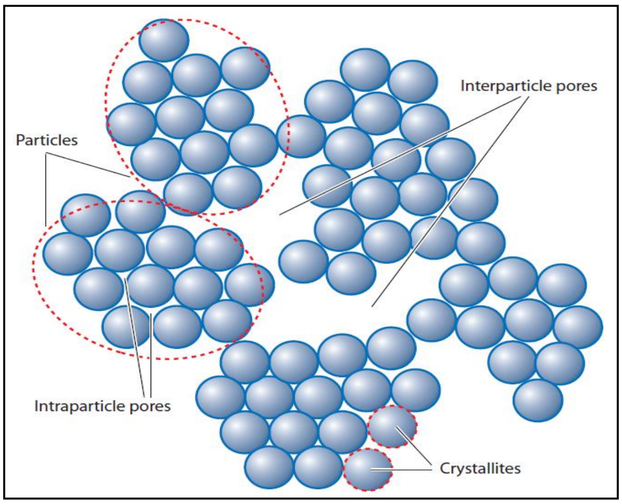

Figure 2.7 A schematic of a powder compact illustrating crystallites agglomerated into particles and two distinct types of porosity [15]

In general, the sintering prefentially describes the densification of a powder. The sintering means the densification on the ground of reduction of surface curvature where the driving force is the reduction of surface energy. The sintering pressure or sintering stress occurs by a surface energy due to particle interaction. The material transport forms sintering neck owing to coalesce of particles by sintering. As shown in Figure 2.7, there are different transport mechanisms. The mass transport mechanism support neck formation. However they cause not main densification. The mechanism 1 and 2 (evaporation and surface diffusion) do not cause densification. Because these mechanisms do not bring the particle centers closer together, contrary cause particle coarsening. So that, sintering can be assumed as competing between particle coarsening and densification.

Mass transport mechanism must be stimulated to maximize densificitaion. The using of high heating rates can support to mass transport mechanism. Surface diffusion that has a low activation energy is more active at lower temperatures than grain boundary or volume diffusion. Thus, high heating rate incline to contribute densification by way of coarsening. Coarsening can be minimized during densification due to rapid heating of powder compact to the desired temperature. The applied pressure causes particle displacement and Figure 2.8 illustrates schematically densification that is based on crystal or particle sliding. The result of applied pressure is a mechanical displacement mechanism and temperature can activate these mechanisms, but should be facilitated by surface and/or grain boundary diffusion. The plastic deformation is the third class of potential densification mechanisms. When the applied pressure exceeds the compressive yield stress of the materials, plastic deformation takes place immediately that is anticipated [15].

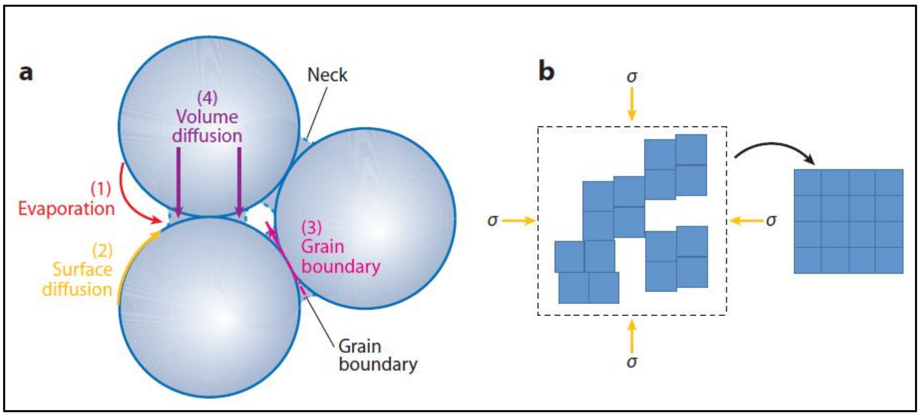

Figure 2.8 (*a*) Mass transport mechanisms that are involved in sintering. (*b*) Schematic of particle or crystallite rearrangement mechanism caused by applied pressures [15]

A main reason for utilizing of external pressure while sintering process is to increase densification by adding a driving force. The external pressure is an especially significant factor for sintering nanostructured powders because it does not directly cause a driving force for grain growth. The pores and any gases in the pores limit the influence of pressure. A longer holding time is necessary to allow diffusion and creep flow controlled mechanism to determine to the final densification that is used with conventional pressure assisted sintering techniques like hot pressing and HIP. The grain growth is a result of the longer holding time. At elevated temperatures, higher pressure can collapse pore structure, induce plastic flow and occur rapid bonding. So that lower holding times can be used at high temperatures and thus grain growth is suppressed [16].

VC, Cr_3C_2, TaC, NbC, MoC or TiC can be used as grain growth inhibitors that limit grain growth during sintering by adding small amounts of them to the starting powder mixtures [17]. The most useful grain growth inhibitors are VC and Cr_3C_2 due to their high solubility and mobility in binder phase at low temperatures [18]. VC and Cr_3C_2

limit the dissolution or reprecipitation of W and C in the liquid phase that will restrict WC grain growth as a result. The influence of VC and Cr_3C_2 on WC grain growth inhibition can be explained by this way [19].

2.2.2 Heating rate and temperatur

As stated above, the short processing time is first advantages of SPS. Especially, a very high heating rate causes the smashingly short sintering times. In general, the heating rates are between 100^{o} C min^{-1} and 600^{o} C min^{-1} in SPS. By comparison with SPS, the upper limit of heating rate for HP is approximately $50^{o}Cmin^{-1}$, but a maximum heating rate of 10–20^{o}C min^{-1} is applied in HP apparatus.

High heating rate present other advantages through alternating the densification process mechanism except for an influential processing time reduction. Generally, bringing the sample to high temperatures ($>0.4–0.5 \times Tm$) causes to minimize the time that a material spends at temperatures at which coarsening mechanisms like surface diffusion are active. So that, one of the main benefits of SPS over HP and pressureless sintering is a high heating rate that is more than 50^{o} C. On the one hand, the study of Shren et al. shows that the density decreases if the heating rate is very high. The reason of this situation can be explanied by the excessively short time subjection of the material [15].

The final density of submicrometer sized powders does not depend on heating rate. In spite of that, the final density of nanometric powders decreases with increasing heating rate. Based on researchers observation, large thermal gradients exist with high heating rates that negatively effect the final density. Thus, the inside of the sample has a great deal of porosity in contrast to the outside of the sample. The certainty of temperature measurements in characteristic SPS experiments is a primary role. The temperature is measured pyrometrically on the surface of the graphite die and thus the inaccuracy in temperature measurements causes the different observations [20].

High heating rates and lower holding times are capable of causing temperature gradients and therefore that causes non-uniform microstructural and mechanical properties of sintered materials due to sintering inhomogeneity. So that, the temperature field in the sintering powder while FAST sintering should be perceived and controlled as far as possible. The temperature distribution in the whole die-sample system should be known to correlate this temperature with the temperature of the sintering powder that is inside the tool.

The thermal and electrical contact resistances between the die constituent and the sample have a major effect on the temperature field, current and power during the heating cycles. The temperature distributions within the tool and the sample are seriously impressed by the electrical properties of the sample. In an electrically conductive sample have much higher thermal gradients in contrast to an insulating sample under same FAST cycles. The current only flows through the punches and die when the sample is an insulator. The radiation from the exposed surface of toll compensates the heating loses. On the one hand, the current principally flows through the conductive sample. So that, the heat loses due to the radiation are not compensated and the temperature distribution in the specimen occurs substantially nonhomogeneous [21], [22]. Most of the Joule's heat will be generated within the three-phase area of die, graphite foil and piston if a non-conductor sample is consolidated. Accordingly, the die thickness and tool diameter affect temperature distribution. Joule's heat is generated inside the graphite bulk and should be convectioned to the overall sample volume. The production of heat should be increased due to increasing sample diameter. Thereby, overheating close to the die will be examined for small dies [12].

Axial temperature gradients can exist in the SPS system with the except of radial temperature distribution. Axial temperature gradients are due to the asymmetric positioning of the plungers in the die. This circumstance is considerably characteristic during SPS study due to initial positioning and/or differences in sliding friction while the early stages of densification.

These gradients are capable of producing inhomonegeties in the sample density and structure as such in radial temperature gradients [23].

Spark plasma sintering (SPS) and other field-assisted sintering technique devices are based on the identical technical mechanisms, but their design is different each other. A current flows directly through the graphite pressing tool that is a part of heating element in both devices. The pressing tool and material, current pulsing and the position of the temperature measurements are the major variations. A pyrometer and/or a thermocouple were used for the determining of temperature. The pyrometer that was oriented the bottom of the upper punch and only 5 mm away from the specimen were used with a measurement range of 450-2200^{o}C in FAST. In SPS apparatus, the range of measurement for pyrometer was between 600^{o}C and 2200^{o}C and was oriented the die surface. The distance of pyrometer from the sample was 10 mm in contrast to FAST.

Alternatingly, a K type thermocouple which can measure the temperature from room temperature until 1100^{o}C was placed in a die hole with a distance of 5 mm from the sample. In each apparatus, the graphite felt was not utilizied due to the measurement position of the circular pyrometer for thermal isolation. For this reason, the heating rates were essentially similar only over 450^{o}C when utilizing the thermocouple and over 600^{o}C with the pyrometer installed in the SPS. Temperature overshoots of 30 ^{o}C up to 40^{o}C in the SPS (at 600 ^{o}C) and 110 ^{o}C up to 130 ^{o}C in the FAST (at 450 ^{o}C) were determined by reason of pyrometer restrictions below a given temperature [24].

2.2.3 Effect of applied pressure

Higher density values were determined at lower sintering temperatures when the sintering process was achieved under higher pressure. The grain size of samples increased slowly with increasing the sintering temperature while solid state sintering. On the other hand, the grain size increased rapidly with increasing the sintering temperature due to producing of liquid Co phase [25].

Higher densification rate is obtained at the identical temperature by the time powders are sintered under an applied pressure. There are several studies grounded on the use of the hot pressing researches. The task of pressure is mechanical and intrinsic. Especially in the event of nanometric powders, the pressure mechanically has a direct influence on particle displacement and the destruction of agglomerates. The intrinsic influence of the applied pressure can be evaluated as a driving force for sintering.

$$\frac{d\rho}{(1-\rho)dt} = B(g\frac{\gamma}{x} + P) \tag{2.6}$$

where ρ is the fractional density, B is a term that includes diffusion coefficient and temperature, g is a geometric constant, γ is the surface energy, x is parameter that represents a size scale , t is time, and P is the applied external pressure. The first term on the right side of Equation 2.6 symbolizes the intrinsic driving force for sintering while the second term represents the intrinsic contribution to the driving force by the applied pressure. The relative greatness of the two terms determine the importance of the applied pressure on sintering behaviour. The relative contribution of the pressure is slight by the time the particle size (related to γ) is small but becomes considerable with increasing particle size.

When the two contributions are equal, the point is presented by:

$$P = g\frac{\gamma}{x} \tag{2.7}$$

The determination of the critical particle size above that the contribution of the pressure to the densification driving force becomes effective is obtained by Equation 2.7.

2.2.4 Effect of current

Electromigration is one of the initial phenomena when the high density current is thought. Electromigration (current-enhanced mass transport) is an area of study due to problems that high-density currents have direct influence on the integrated circuit (IC) industry. Although low current densities are utilizied, the currents which are used in IC interconnects can be approximately in 10^6–10^7 A cm^{-2}. In SPS/FAST currents are very high, however the samples are in tendency to be much larger in cross-sectional area for lower current densities. In a SPS/FAST investigation, determination of the true current densities is excessively difficult. The calculation of quantity of the current during densification stage is very diffucult due to the potential current paths such as die wall and plunger contacts and sample that frequently changes conductivity [15].

The graphite die and conductive sample are heated by Joule heating by a current that pass through them. The other role of pulsed DC is composing of plasma with the except of heating. The production of plasma occupied through the ionization of metal atoms such as Al, W and Cu or gaseous molecules and atoms like O_2, N_2, H_2O, O, N, Ar, and He. The plasma is capable of causing a cleaning influence on the surface of the particles and improves the sintering conditions. One muss review the presence of plasma with applied pressure and the stage of sintering. The occurence of wide bond areas between the particles depends on these parameters. A discharge probably occurs in conducting powder at the beginning of sintering process. When the amount of contacts increases due to the applied pressure and sintering, the possibilty of discharge becomes small. If non-conductive powders are sintered, this situation becomes more complex [11], [20].

FCT SPS device (Type HP D 25/1, FCT Systeme, Rauenstein, Germany) mounted with a 250 kN uniaxial-press. One can evacuate the process chamber down to 0.05 Pa. A pulsed DC up to 8000 A at a voltage up to 10 V over the electrodes to the tool set that includes the sample is obtained by the power supply. There are graphite adaption between the punches and the water cooled electrodes. One can generate a pulsed and a constant DC with on/off cycles of 0-255 ms [26]. When the current-delivery system was substantially changed by considerably increasing pulse frequency or by changing the pulse shape, pulsing could act a part. The pulsing in the most of SPS/FAST tests have a little or no effect [15]. Different works have pointed out that pulse pattern had no influence on densification or grain growth [27].

2.3 Proporties of WC-Co hard metals

The cemented carbides consisting of WC grains bound with Co phase have been utilized for rock drill tip, cutting tools and other wear resistant parts during the last several decades. The influence of Co content and the addition of different types of cubic carbides (grain growth inhibitors) have been researched for enhancing the mechanical properties of WC-Co cemented carbides [25].

2.3.1 Hardness

Tungsten carbide–cobalt hard materials (WC–Co) arise from a high volume fraction of the ‘‘hard’’ hexagonal WC phase embedded within a soft and tough Co binder phase.

When the volume fraction of Co increases, the fracture toughness increases in contrast to hardness and wear resistance (Figure 2.9) [28].

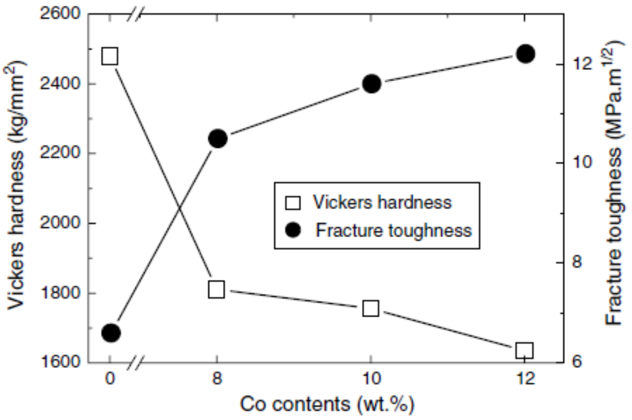

Figure 2.9 Vickers hardness and fracture toughness as a function of Co contents in WC and WC–Co hard materials [28]

The hardness of WC-Co cemented carbides increases with decreasing WC grain size. The reductiont of WC grain size relevants to the decreasing WC particle size in the raw material (Figure 2.10) [29].

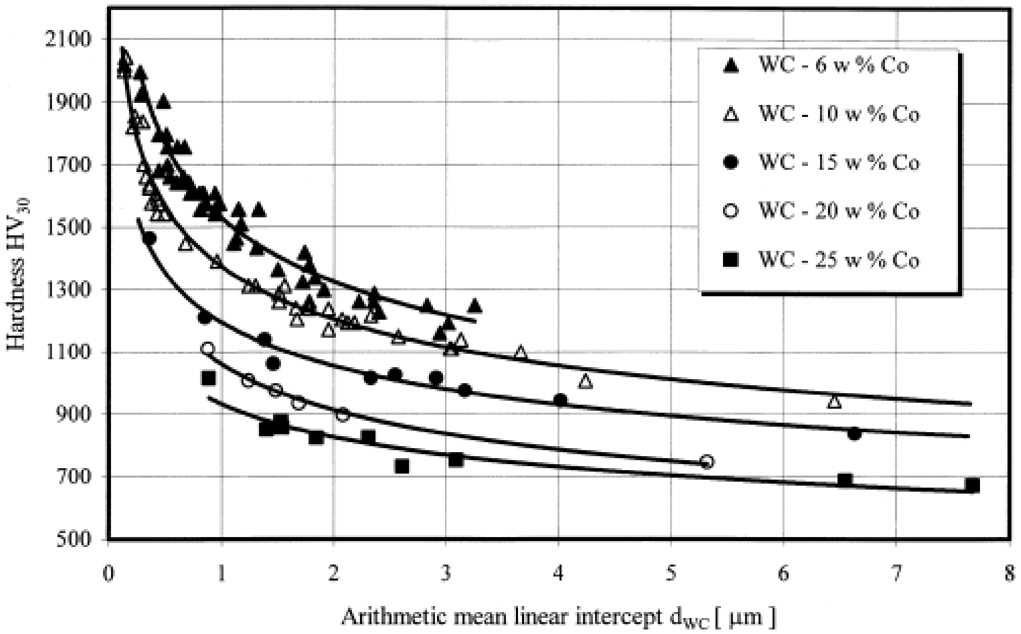

Figure 2.10 Hardness HV30 depending on WC arithmetic mean linear intercept d_{WC} [30]

A model to measure the hardness of cemented carbides using a continuous volume concept and rule-of-mixtures was offered by Lee and Gurland [31]. A revised hardness model which takes differences in the constraint factors of WC-Co for WC-Co cemented carbides can be offered by replacing the flow stresses of WC-Co cemented carbides, the WC particles and the Co phase in Lee and Gurland's equation with their hardnesses. By Equation 2.8, the hardness of WC-Co cemented carbides can be calculated.

$$H_{CC} = 1.205 H_{WC} V_{WC} C + 0.9 H_{Co} (1 - V_{WC} C) \tag{2.8}$$

where H_{CC}, H_{WC}, H_{Co} is the hardness of the cemented carbides, the WC particles, and the cobalt matrix, respectively.

A Hall-Petch relation is suitable to calculate hardnesses of the carbide and the cobalt and it is as follows:

$$H_{WC} = 13.5 + \frac{7.2}{\sqrt{d}} \tag{2.9}$$

$$H_{Co} = 2.98 + \frac{3.9}{\sqrt{\lambda}} \tag{2.10}$$

where d is the particle size of carbide and λ is the mean free path of the binder phase. The unit of the hardness is GPa [32].

Whereas, the Equation 2.8 predicts that while decreasing the WC grain size to zero, the hardness of cemented carbides increases consistently to infinity. This relation can create problems for calculation of the hardness of ultrafine or nanocrystalline WC-Co cemented carbides. In this case, Equation 2.11 is offered for the hardness of WC-Co cemented carbides, that is:

$$H = \frac{2\pi H_{O,Co}}{\left(\lambda/\sqrt{\lambda^2 + d^2}\right) + (1 - 2\upsilon)\ \ln\left(1 + \left((\sqrt{\lambda^2 + d^2}/\lambda\right)\right)} \tag{2.11}$$

If the WC grain size is larger than 0.7 μm, one can use both the Hall-Petch relationship an the offered model to measure hardness values of the WC-Co cemented carbides. On the one hand, only the offered model can be used to measure hardness when the WC grain size is below 0.7 μm [33].

2.3.2 Fracture toughness

The mechanical properties of tungsten carbide-cobalt materials should be well known because of their use is really restricted by their brittleness. Brittleness causes low toughness and high sensitivity to microstructural defects. When the volume fraction of cobalt V_v (Co) increases, a permanent increase of K_{Ic} is recognized. Its value should increase with the ductility of the material because the critical stress intensity factor symbolizes the resistance to crack propagation. If the volume fraction of cobalt increases, the influence of the mean diameter of the carbide crystals is more explicit. So that, the toughest materials have the coarsest grain sizes [34].

It is well known that the fracture toughness of cemented carbides is inversely proportional to the hardness and that the hardness is inversely proportional to its grain size. When the grain sizes are excessively fine, the relationship between hardness and fracture toughness might not be linear. For this reason, a finer grain size typically incurs lower fracture toughness. Whereas, the strengthening mechanims of nanostructured metal alloys and ceramics are diversified due to the large volume fractions of grain boundaries. The deformation mechanisms subject to diffusion-controlled processes and grain boundary processes. The motion of cracks is limited by grain boundaries in polycrystalline metals this provides better fracture toughness. Hence, it is assumed that when WC grain sizes attain nanoscale the fracture toughness of WC-Co cemented carbides would increase [16].

Figure 2.11 shows the fracture toughness of different WC-Co grades. At a certain hardness, there is a remarkable gap between the highest and the lowest toughness values. The relationship between toughness and hardness of individual alloys depends on changing in composition and microstructure [35].

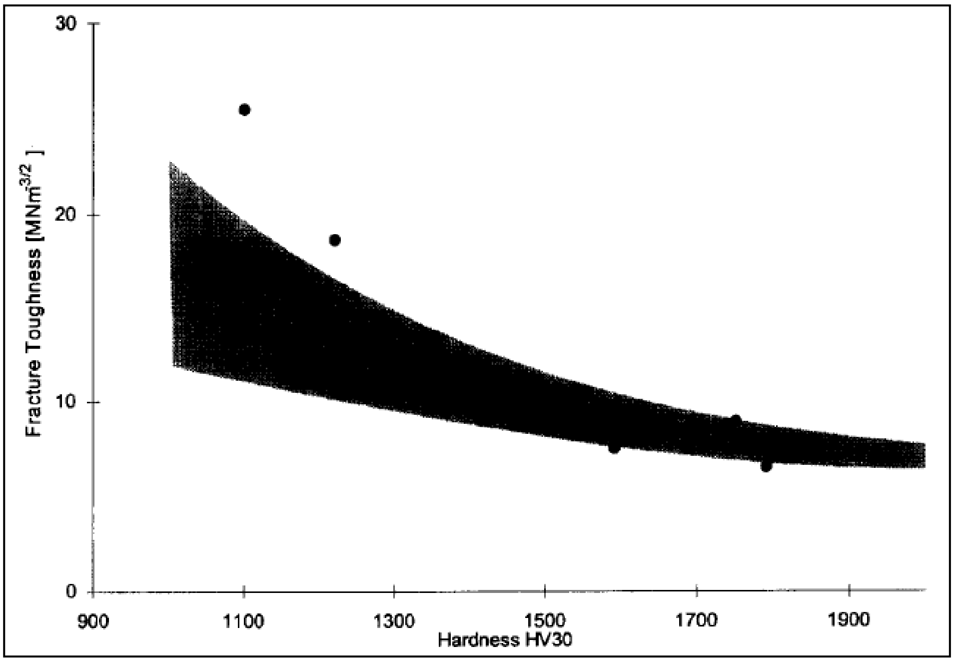

Figure 2.11 Fracture toughness vs hardness for a range of hardmetals [35]

Palmqvist beginned and improved the opinion of testing the fracture toughness of cemented carbides. According to Palmqvist, one can calculate it by the sum of the crack lengths at the four corners of a Vickers hardness indentation.

The residual stresses on ground surfaces of cemented carbides can be measured. Dawihl and Altmeyer used the crack lengths that relevant to the indentation to measure it. Exner identified a crack resistance (W) and grounded on the observed linear relation between indentation load (P) and the sum of the radial crack lengths at the corners of the Vickers hardness impression:

$$W = \frac{P}{4\bar{a}} \tag{2.12}$$

Equation 2.12 should be changed for higher binder content alloys (more than 10 %), due to to Ogilvy et al. and Perrotts experimental results.

$$W = \frac{(P - P_o)}{4\bar{a}} \tag{2.13}$$

Niihara, Warren and Matzke have individually offered a relation of the form:

$$K_{Ic} = \beta(HW)^{1/2} \tag{2.14}$$

the constant β in Equation 2.14 has a very simple interpretation in terms of the indenter geometry ,ψ, and the Poisson's ratio, υ. For $\upsilon = 0.22$ (typical of WC alloys) and $2\psi = 136^o$ for the standard Vickers indenter $\beta = 8.89\text{x } 10^{-2}$ [36].

Shetty et al. and Spiegler et al. calculated a value for K_{Ic} for each indentation load using the expression:

$$K_{Ic}=A(H)^{1/2}(P/l)^{1/2} \tag{2.15}$$

where A is a constant, H is the hardness, expressed in N mm^{-2}, P is the load in N and l is the total crack length in mm. The value of the constant A is 0.0028 for the toughness K_{Ic} to be expressed in MN $m^{-3/2}$ [37].

Basically, three distinct modes of indentation fracture are available in brittle solids. When a curved indenter contacts to the sample surface, Hertzian cone cracks are formed. On the one hand, median vents or lateral vents that are cracks can occur by contact with a sharp indenter and nucleate at the tip of the indenter and propagate into the underlying material. Figure 2.12 shows the two types of median vents (*Palmqvist cracks* and *median cracks*).

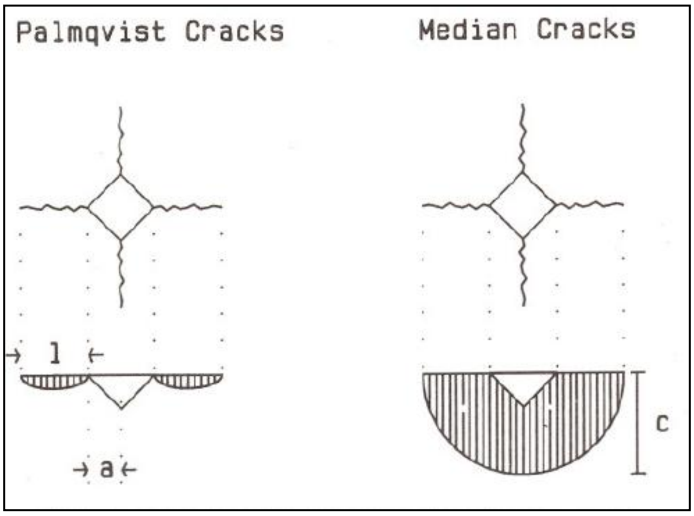

Figure 2.12 Crack geometries of Palmqvist and median cracks [38]

Lateral vents tend to cause macroscopic chipping around the indentation and propagate at a small angle to the surface. The very brittle materials such as glasses tend to are in tendency to compose lateral vents. However, median vents are formed by materials which show some plasticity. The occurence of lateral vents is limited by cyclic loading in cemented carbides, particularly for hard grades or stress corrosion cracking in aggressive atmospheres. Only median vents take place in WC-Co alloys under normal conditions [38].

Both of Palmqvist ($0.25 \leq l/a \leq 2.5$) and median crack types ($c/a \geq 2.5$) are idealized. For this reason, the differences from the actual crack shape in cemented carbides are small. Hence, both Palmqvist and median crack types can be taken in to account [39].

Surface preparation is very important for the fracture behaviour of cemented carbides. The surface of cemented carbides should be efficiently grounded and polished. While several steps of surface preparation, one should use diamond as abrasive [40].

2.3.3 Strength behaviour

Bending strength, hardness and fracture toughness are predominantly used to characterize the mechanical behaviour of hard metals. In the literature, material properties such as yield and ultimate tensile strength are not determined owing to the low ductility and the high hardness. So that, the detection of reliable material knowledge is a hard study. Generally, the inequality in tested effective volume and the non-linear stress distrubution in the bent samples that are relatively deformed plastically before fracture cause the higher values of ultimate tensile strength and yield strength in bending than in uniaxial testing situation [41].

In [42], the average WC grain sizes of ten different hard metal grades were ultrafine (0.2 to 0.5 μm), submicron (0.5 to 0.8 μm) and fine (0.8 to 1.3 μm). On the other hand, the cobalt binder phase content was varying between 6 to 12 wt. % to realize static uniaxial tension and compression tests. According to experimental results, the tensile strength values of studied hard metal grades were between 1400 and 2900 MPa. In spite of that, the compressive strength ranging from 5000 to 8500 MPa. Beginning of plastic deformation that can be characterized by the $Rp_{0.05}$ yield strength occurs approximately between 2400 and 5700 MPa.

The content of the binder phase are very important for the mechanical behaviour of ultrafine hardmetals under droningly increasing and changing bending loads. The fatigue sensitivitiy under cylic loads and the strength of ultrafine-grained hardmetals depends on the binder content. The ultrafine grained hardmetals which include pure Co binder phase show high bending strength values and fatigue sensitivity. On the one hand, the hardmetals that consist of complex binder systems presented lower bending strength values and fatigue sensitivity. This sitiuation is indicative of that the ultrafine grained hardmetals with pure Co and complex binder systems have different failure mechanisms [43].

In [44], the mechanical properties of WC-Co cemented carbides were performed at different hard metal grades varying in average WC grain size from 3 to 30 μm and cobalt binder content ranging from 5 to 20 wt. %. In accordance with test results, the samples with larger WC grains (20-30 μm) are ductile. Conversely, the samples with smaller grains (3-6 μm) show brittleness. The Young's modulus value of the samples with WC grains of 3-20 μm is 577 GPa and 523 GPa for a grain size of 30 μm. As a result, WC grain size have influence on the Young's modulus. The compressive strength decreases with increasing grain size till 20 μm, but a decrease did not determine for a grain size of 30 μm. From investigation of various Co contents for specimens with a WC grain size of 20 μm, it was found that the ductility was retained, regardless of the Co content. When the Co content increases the Young's modulus and compressive strength decreases. So that, the mass ratio of WC to Co could be used for the determination of the Young's modulus of WC-Co cemented carbides with WC grain size of 20 μm or less, but it is calculated by different factors for larger grain sizes.

The microscale structure of a brittle material depends on compressive loads. The formation of subcritical crack propagation in hot-pressed ceramics depends on the strain rate. That is the reason why their compressive strengths are effected by the low strain rates (up to 10^2 s^{-1}). Inertial effects and dynamic crack propagation have an influence on the compressive strength of a brittle material in the high strain rates (~10^2–10^4/s). When these high stain rates are applied during the dynamic loadings, the propagation of microflaws is limited by inertial effects. As a consequence, some slip within grains (microplasticity) and an extra toughening mechanism occur. The dynamic failure behaviour is affected by micro-fracture and microplasticity in the ultra-high strain rate regime (~10^4–10^7/s) [45]. The peak strength increases with increasing strain rate, although the fragment size decreases [46]. The fragment size depends on the damage evolution mechanism and the microstucture of material. The damage behaviour is influenced by of strain rate, the microstructure and the loading rate. The strain rate, the microstructure and the loading conditions govern the fragment size. When the lateral confining pressure is increased, the fragment size decreases due to the coalescence of tension cracks arising from microflaws that are closer to one another. As a result of increasing strain rate, the fragment size decreases based on the coalescence of compression-induced tension cracks arising from smaller flaws [47].

One can describe the elastic limit under compression and theoretical compressive strength of WC-Co cemented carbides by following relationships in parallel with microstructure parameters.

$$R_{cm} = \left[2.551 + 0.108 V_{Co} - 1.238 V^2{}_{Co} + \frac{1}{\sqrt{d_{WC}}} (5.591 - 0.877 V_{Co} - 3.046 V^2{}_{Co}) \right] \sqrt{C} \quad (2.16)$$

$$R_{cp\,0,05} = C \left(1.65 + \frac{3.5}{\sqrt{d_{WC}}} \right), V_{Co} \leq 0.2 \quad (2.17)$$

Equation 2.16 and 2.17 can be used from ultafine to coarse-grained hardmetals [48].

2.3.4 Elasticity

Figure 2.13 represents the effect of the binder phase content and the grain size of the WC on yield strength Rp$_{0.05}$, Rp$_{0.1}$ and Rp$_{0.2}$ under compressive loading.

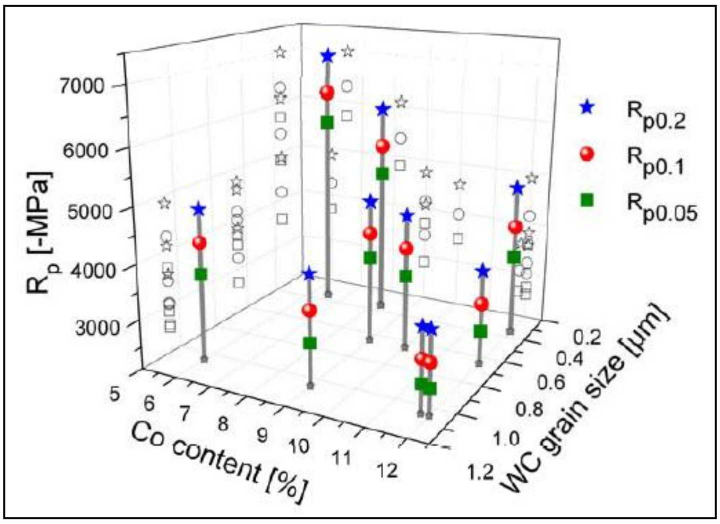

Figure 2.13 Effect of binder content and WC grain size on yield strengths Rp$_{0.05}$, Rp$_{0.1}$ and Rp$_{0.2}$ in compression [42]

As it can be seen, when the mean WC grain size and binder phase content decrease, the values of the flow stress increase remerkably. The result of this can be clarified by the increased resistance dislocations have to pass over when moving from inside of the thinner binder channels. Channels that are between WC grains occur larger and the restriction for the dislocation movement decreases in grades of identical WC grain size whereas increasing binder content.

When WC grain size is increased as the binder content is constant, the identical situation becomes [42].

Young's modulus subject to WC grain size which ranging from 0.6 to 5µm for WC-Co (6,10 and 16 wt%) carbides. Because the independency of shear modulus of the carbides on the WC particle size is similar. Generally, the WC grain size have not an effect on elastic modulus of the alloys. Shear modulus and Young's modulus of the alloys do not depend on the carbon content in the two-phase range (WC+β). On the other hand, the carbon content have an significantly influence on the transverse rupture strength and Young's modulus indistinctly decreases if η or free graphite phase takes place [49].

The yield strength of a WC-Co alloy can be calculated by Equation 2.18 if its WC grain size ranging from 1.1 µm to 5.5 µm and the volume fraction of cobalt phase is between 6.08% and 63.7% [50].

$$E = \frac{80 + 30 \cdot {d_{WC}}^{-1/2}}{1 + 8.3 \cdot V_{Co}} \tag{2.18}$$

2.4 Deformation and failure behaviour

In general, it is assumed that the binder phase is continuous, but the continuity degree of the carbide phase is questionable. An assumption presumes that the structure of the sintered WC-Co alloys includes dispersed carbide particles that embedded in a continous binder phase. Each carbide particle is disciminated by thin binder film. An accordance with this assumption, the plastic deformation of WC-Co alloys just depend on the binder phase. This theory is supported by a lot of studies and the binder mean free path is used to determine the strength of cemented carbides. There is an other hypothesis that accepts the existing of a continuous carbide skeleton. According to this hypothesis, a significant plasticity in the carbide is necessary for the plastic deformation of the alloy. Because, the deformation of the carbide skeleton should conform with the binder phase.

The residual stresses which can be microscopic or macroscopic play an important role in cemented carbides. Microscopic residual stresses are dependent on the thermal expansion coefficient which is different for the phases. The residual stress of the cobalt phase has not been determined, but it is relatively accepted that it is in tension. As a consequence of surface preparation process such as grinding and polishing, macroscopic residual stresses take place. Close by surface, the WC and cobalt binder phase are in compression. On the other hand, in the subsurface fields, the compressive stresses are stabilized by tensile stresses. The depth of stress field that is in compression is about 20-30 μm. The stresses due to the difference in thermal expansion coefficent of phases are generally much smaller than residual stresses [4].

The material is subjected to elastic, elastic-plastic and completely plastic deformation under an indentation load. The mechanisms of plastic deformation consist of the binder phase deformation and other mechanisms like slip bands through the carbide grains, sliding throughout intercarbide grains and the microcracks formation. The relation between microcrack number density and indentation strain is investigated. In this case, the plastic deformation of WC-Co cemented carbides is considerably dependend on microcracking. There are several paths for microcracks motion. These are transgranular cracks within WC grains, intergranular cracks through WC/WC grain boundaries and cracks throughout the WC/Co interface [51],[52].

The type $\{1\bar{1}00\}\langle 11\bar{2}3\rangle$ slip system is major in the carbide. As such a combination can produce just four independent strains and one of them is necessary for the compossible plastic flow in a polycrystalline aggregate. Nominately, WC is not compressible along $\{000l\}$. There is a model which is offered for probability of the a grain boundary failure. The result of experimental studies on either cracked or untracked grain boundaries verifies the theoretical prognosis. A crack occurs as a result of influence of the stresses on a boundary and incompatible deformation of neighboring grains [53].

The presence of the binder phase in sintered WC-Co cemented carbide shows fcc modifications that is obtained. Nevertheless, at room temperature, the fcc modification is not stable. So that, there are many stacking faults as well in the undeformed condition. An energy decrement is acquired as a consequence of the fcc→hcp transformation. Because Co dissolves W and C as a solid solution that retards the martensitic transformation and reduces the Ms temperature. The considerably rigid skeleton of WC grains has an influence on restriction of the transformation when a shape change is consisted of by the martensitic transformation. Micro-lamellae of hcp material (two or four atom layers thick) has nearly the same meaning as stacking faults in the fcc modification of the binder of sintered WC-Co cemented carbides [54]. Pure bulk cobalt has the stable hcp crystal lattice under 418^{o} C. The reason why the fcc high temperature structure is stabilised in the binder phase of cemented carbides to the room temperature and below is that there are residual stresses, dissolved tungsten and carbon. The tranformation from fcc to hcp structure in the course of mechanical testing or application is observed in investigation [55].

Binder phase of conventional and nanostructured composites are mostly different from each other. Conventional composites include less tungsten content in the binder phase than nanostructured composites. In the nanostructured composite, it increases both volume fraction of the binder phase and the ratio of FCC/HCP of the cobalt. The solubility of WC that stabilizes the FCC phase of cobalt following cooling from sintering temperature is promoted by the small size of the WC grains in the nanostructured composite [8].

The four types of defect in the binder phase occur in course of plastic deformation, these are:

(i) dislocations

(ii) stacking faults (SFs)

(iii) twins

(iv) regions where the cubic lattice (stabilised to room temperature by stress and compositional effects) is transformed to the stable hexagonal lattice (SFs are precursors of the hexagonal lattice; thus, types (ii) and (iv) are related).

TEM can determine these defects when the visualization situations are suitable [55]. It is appeared that four types of fracture paths in WC-Co as stated in [56]. The transgranular fracture within carbide crystals C, fracture near to the carbide/binder interface β/C, intergranular fracture throughout carbide grain boundaries C/C and the transgranular fracture through the binder phase β are types of fracture paths.

It is mostly known that a great deal of fracture energy is dissipated in path β. Most researchers have agreed the fracture energy is not dissapated in path β/C. Because a crack propagation in path β/C interface would absorb only little energy. After compression tests and on the tensile face of TRS specimens, it has been observed in WC that both transcrystalline and intercrystalline fracture progress fundamentally in a brittle manner even though signs of plasticity (slip lines, glide steps) in the carbide phase. The contribution of paths C and C/C to fracture energy owing to high volume fracture of carbide phase must be considered. Hence, quantative data that consist of the relative amount of all four types of fracture paths are remarkable.

Evans et al. have firstly idendified that the process zone of arrested cracks in WC-Co alloys which are the multiligament type. A continous are in which the binder regions stay as isolated ligaments is constitued by the crack that initially stretchs along the carbide phase. The ligaments are stretched till dimple fracture rupture them if the crack opens. It is observed that an intensive plastic deformation in the binder phase occurs close to crack [57].

According to fracture surface observations, hole nucleation and growth break the ductile regions in the WC/Co system. In additon, it is schematically illustrated in Figure 2.14 that the hole spacing seems to rest on the location of the crack plane in accordance with the center of the ductile enclave [58].

Dilated zones or shielding from enclaves undergo phase transformation. On the other hand, a constant reduction in regional stress intensity or at least for a stable equilibrium zone size is generated by microcracking or void formation [59]. The average intercept of the binder phase is limit superior for the average size of the plastic region. The average linear intercept in the binder phase is usually larger than the actual extension of plastificied binder phase [56].

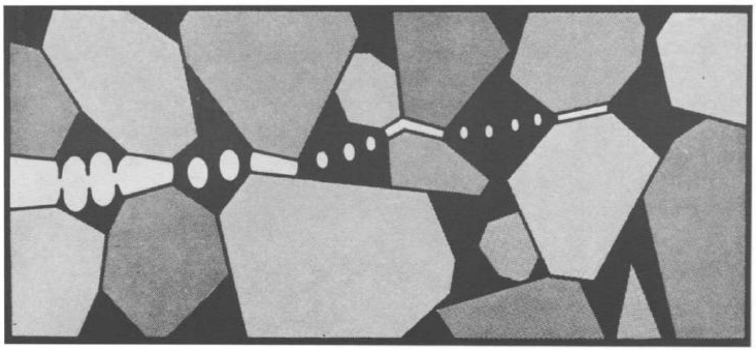

Figure 2.14 A schematic representation of the bridging process [58]

When the grain size of the hard phase is under 40 nm, the lower fracture toughness occurs due to free form of dislocations and brittleness. Even if the cobalt is distributed in thin layers among fine carbide grains, the cobalt looses the skill that is necessary for the stopping crack propagation. Gille used to characteristic behaviour of cobalt which presents brittleness below a critical mean free path for reporting mechanical properties of ultra fine hardmetals. The fracture toughness of super-ultra fine nanocrystalline hardmetals would be comparatively low. On the one hand, the strength can be very high due to small defect size [60].

According to investigations, the microcracks can form during plastic deformation when WC-Co materials consist of larger average WC grain size, larger mean free path and lower contiguity of the WC phase. Lower hardness and higher fracture toughness causes higher microcrack number density. The mechanism of crack shielding by softening the material in fracture zone causes the microcracking toughens in WC-Co cemented carbides [51].

CHAPTER 3

EXPERIMENTAL METHODS

WC powder (H.C. Starck) and Co powder (Half Micron Powder/Umicore) were used as raw materials. The raw powders were prepared in inert gas atmosphere (Ar) in a Glovebox UNIlab (mBRAUN) (Figure 3.1). 5,4 g Co powder is necessary for 45 g WC-12Co powder.

Figure 3.1 Glove box, TU BA Freiberg

Table 3.1 shows the raw material properties. According to Equation 3.1 the theoretical density can be calculated [61].

Table 3.1 Specific surface area and particle size of Co and WC powder

	S_{BET} [m^2/g]			
Powder	Manufacturer Information	Test Result	$\bar{d}_{Par}$ [nm]	$\bar{d}_{Par,\ corr}$ [nm]
Co-Pulver	4.0	3.745	181	219
WC	3.8-4.2	3.892	98	118

where S_{BET}, $\bar{d}_{Par,}$ $\bar{d}_{Par,\ corr}$ is the specific surface area, mean particle size and corrected particle size of WC and Co particles according to BET analysis, respesctively.

$$\frac{100}{\rho_{th}}=\frac{x_{WC}}{\rho_{WC}}+\frac{x_{Co}}{\rho_{Co}}, \qquad (3.1)$$

ρ_{Co}=8.85 g/cm^3, ρ_{WC}=15.7 g/cm^3[62]

5-6 ml of cyclohexane in order to the wet milling for each 10 g powder were added (C_6H_{12}). The raw powders were mixed by planetary ball milling (Figure 3.2). Diameter of the WC milling balls was 5 mm. Milling die was made of WC, (Figure 3.3), to avoide impurities and wearing during the ball milling process. The ball to powder weight ratio 6:1 was used.

Figure 3.2 Fritsch Pulverisette 6, TU BA Freiberg

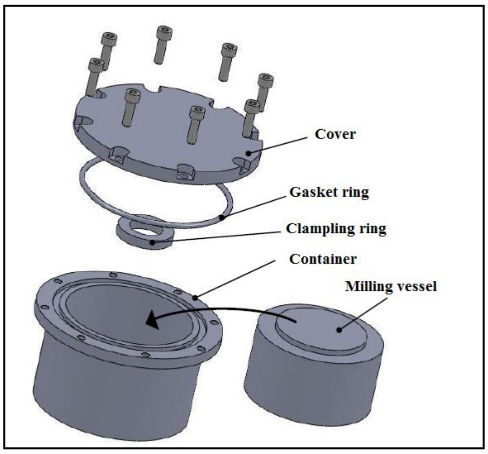

Figure 3.3 Schematic design of the milling die [9]

The most favorable number of rotation for cyclindrical powder mill at dry milling is suggested. According to Equation 3.2 the most appropiate speed depends on balance between centrifugal and gravitational force [63].

$$2{\cdot}m{\cdot}\text{л}^{2}{\cdot}N_c^{2}{\cdot}d=m{\cdot}d \qquad (3.2)$$

The rotation speed of the powder mill (N_c) can be calculated by the following equation.

$$N_C = \frac{42.3}{\sqrt{d}} \tag{3.3}$$

In Equation 3.3 d means diameter of the milling die (in m). The optimum mixing of the powder is obtained at 75% of N_C. In this study diameter of milling die is 0.065 m and optimum rotation speed is about 130 rpm. However, this model considers only dry milling process. These parameters lead to energy input and friction. At the time of the ball milling process, 10 minutes waiting period was applied for each repetition by reason of overheating. The applied milling process was 20/10/25, 20/10/50 and 20/10/75 to observe effect of milling time. This representation consists of milling time (min), breaking time (min) and repetition, respectively. Subsequently, the milled powder mixture was dried in glovebox for at least 24 hours to evaporation of cyclohexane. Dried powder mixture was put into the graphite die after the sieving.

3.1 Sintering Process

The sintering tests were carried on WC-12Co powder. The influence of milling time on the microstructure and the mechanical properties were described by the cemented carbide samples. The sintering experiments are variaton of sintering time (t_{sinter}), sintering temperature (T_{sinter}) and cooling process. A variation of the sintering time 5, 6 and 7 min and the sintering temperature between 1050 ^{o}C and 1150 ^{o}C was performed. The influence of the cooling rate was researched at the sample 967, 974 and 975. The samples were prepared at same conditions and were sintered at 1050^{o} C. The cooling rate was applied 100 K/min, 150 K/min and 200 K/min, respectively. A pulsed DC passed through the tool and the sample during the controlled cooling process.

The sintering process was performed on SPS device (FCT System Ltd. HP D 25/1) (Figure 3.4). Die was chosen as a graphite mold which has inner diameter of 20 mm. Graphite foil was used to eliminate to adhesion of powder and sintered samples to graphite mold. Also, graphite foil prevent powder from the punches. This process could performed in air atmosphere. After graphite foil was loaded into the graphite mold, approximately 22 gram of WC-Co powder were filled into graphite mold in the glovebox. WC-Co powder was precompressed within the graphite mold with a hand press until the first deflection of the pointer on the force display. At the beginning of the sinter process, the graphite mold was felted and fixed centrally. So, initial press could be applied to graphite mold. The SPS process was applied at specified temperatures. Figure 3.5 is representing temperature and pressure force curve of sintering process.

Figure 3.4 SPS device, TU BA Freiberg

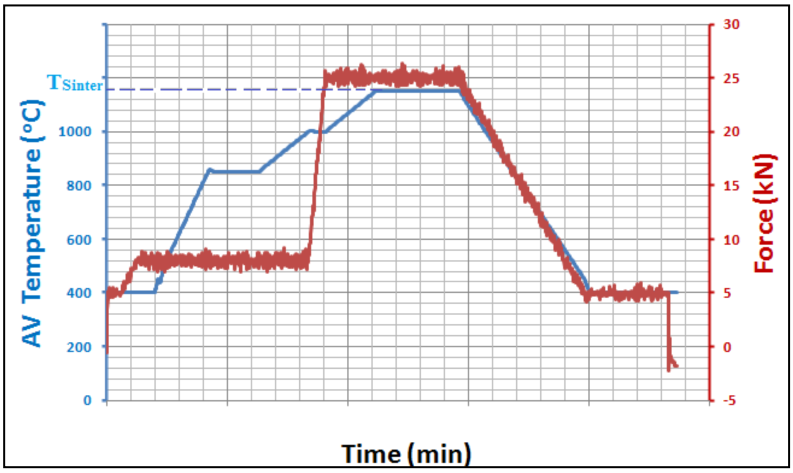

Figure 3.5 Schematic temperature and compression force profile during sintering

The entire process of densification using the SPS technique consists of four major control stages. These are vacuuming, pressing, power application and cooling down. The SPS process proceed with the closing and evacuating of process chamber. The temperature was measured by pyrometer that is only a few millimeters above the sample material. The pyrometer measure temperature that is above the 400 ^{o}C. The vacuum pressure was applied during the entire sintering process to remove gas occurring. Then the temperature was increased to 850 ^{o}C. This temperature was hold for 3 minutes. At this stage the pressure force of approximetely 8 kN was applied for precompression of the powder and removing of adsorbed gases. Then, the sample was heated up to sintering temperature. At this section, heating rate was realized between 117-133

K/min. At the same time, the pressing force was increased to 25 kN. Maximum pressure and the sintering temperature was applied between 5 and 10 minutes at the sintering temperature. Following this was cooling of the tool and the sample. The cooling process is realized by heat conduction over graphite adapter, water cooled steel punches and as a result of heat radiation. Table 3.2 is representing a survey of the milling time and sintering parameters to the produced SPS samples.

Table 3.2 Milling and sintering parameters of samples

Sample Number	**$t_{Milling}$ (min)**	**$T_{Sinter}[^{o}C]$**	**t_{Sinter}[min]**	**$\dot{T}_{Cool}$ [K/min]**
919	1000	1150	5	93.3
921	1500	1150	5	93.3
941	1000	1150	6	100
942	1000	1150	7	100
943	1000	1100	5	100
946	1000	1100	6	100
947	1000	1100	7	100
966	1000	1150	5	100
967	1000	1050	5	100
974	1000	1050	5	200
975	1000	1050	5	150

The height of the samples is about 5 mm (with burrs) as a resultant of sintering process. Then the sandblasting was performed for surface cleanliness.

3.2 Sample Preparation

Sintered compact samples were quartered by a diamond cutting disk to warm embedding (Predopress/Struers) (Figure 3.6). The warm embedding process was realized at a temperature of about 170^{o}C and a pressure of 15 kN. For this purpose, the granules of WEM Epoxy and WEM Phenol were used. Also, three minutes preheating, six minutes holding and six minutes cooling were applied while processing.

Figure 3.6 Hot embedding press, TU BA Freiberg

The grinding and polishing was done at “Abramin” and six samples were used for this process (Figure 3.7). The sub-steps are illustrated in Table 3.3.

Figure 3.7 Grinding, lapping and polishing machine, TU BA Freiberg

After grinding and polishing, etching of samples was performed with Murakami etching agent (10 g KOH+10 g $K_3[Fe(CN)_6]$+100 g H_2O). Following the etching time of about five seconds, water and Ethanol was carried out to clarify etching agent.

Table 3.3 Individual steps of grinding and polishing WC-Co

Sub-Step	**Disk**	**Grinding**	**Suspension**	**Additive**	**F (N)**	**n (min^{-1})**	**t (min)**
1	Piano	120	-	Water	150	300	Sufficiently
2	Allegro	-	DP-15µm	Lubricant	150	150	2
3	Allegro	-	DP-6µm	Lubricant	150	150	2
4	Dac	-	DP-6µm	Lubricant	150	150	6
5	Dac	-	DP-3µm	Lubricant	150	150	3
6	Nap	-	DP-1µm	Lubricant	120	150	4

3.3 BET Method

BET surface analysis named after initals surnames of developers: Brunauer, Emmett and Teller. There is a standard of ISO 9277 to determine surface area and porous dispersion. The process is based on measuring the amount of physisorbed gas. BET theory aims to explain the physical adsorption of gas molecules on a solid surface and serves as the basis for an important analysis technique for the measurement of the specific surface area of a material. The weak connection of monolayers depend Van-der-Waals forces of gas molecules that change reversible by temperature and pressure. The determining of the specific surface depends on adsorption and desorption of nitrogen that is at pressure reduction and a constant temperature of 77 K on the surface of solid [64],[65]. Figure 3.8 shows the apparatus of BET method.

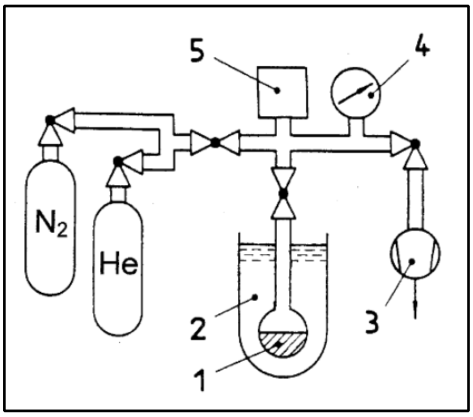

Figure 3.8 Schematic diagram of BET system. 1) Sample, 2) Dewar flask with liquid nitrogen 3) Vacuum unit, 4) Manometer, 5) Gas burette [63]

The calculation of the monolayer capacity (n_m) is possible with aid of the adsorption isotherm and via the BET equation.

$$\frac{p/p_0}{n_a \cdot [1-(p/p_0)]} = \frac{1}{n_m \cdot C} + \frac{C-1}{n_m \cdot C} \cdot \frac{p}{p_0} \tag{3.4}$$

The availability of the BET equation is limited to a range of relative pressure p/p_o between 0.005 and 0.3. Specific adsorbed amount is indicated n_a. In Figure 3.9 the linear intercept of the adsorption isotherm is shown schematically [63].

The value of the slope (b) and the y-intercept (a) are used to calculate the monolayer adsorbed gas quantity (n_m) and the BET constant (C). The following equations can be used.

$$n_m = \frac{1}{a+b} \tag{3.5}$$

$$C = \frac{b}{a} + 1 \tag{3.6}$$

According to ISO 9277, calculation of specific surface area a_S is possible using nitrogen as the adsorbate.

$$a_s = 9.76 \cdot 10^4 \cdot n_m \tag{3.7}$$

On the basis of the specific area a_S one could make an estimation about particle size through density of absorbed materials. The correlation is showned in Equation 3.8.

$$d_{BET} = \frac{6}{a_s \cdot \rho} \tag{3.8}$$

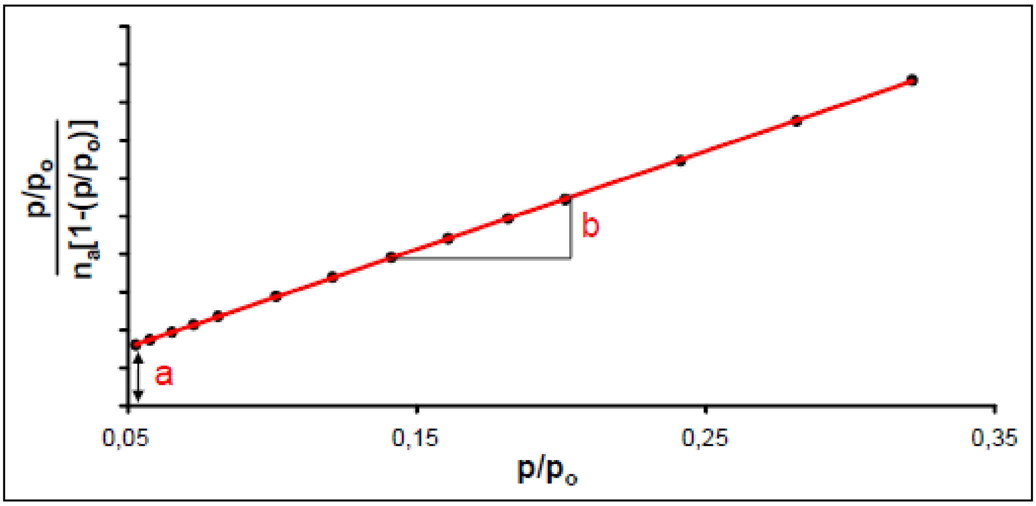

Figure 3.9 The linear region of the adsorption isotherm

3.3.1 BET surface analysis including the fractal dimension

At previous section, a calculation of material particle size was described according to BET method. However, this method assumes that the particles are spherical and atomically smooth. So that, the adsorption energy is equal for all particle surface and covering degree is not considered. The aim of the fractal dimension is creating a roughness factor for topography of real surface area [66], [67]. This is based on Equation 3.9.

$$\lg V = \text{Const} + s \cdot \lg\left[R \cdot T \cdot \lg\left(\frac{p_0}{p} \right) \right] \tag{3.9}$$

The V is the specific volume of the adsorbent. The characteristic value s is a function of fractal dimension. The roughness factor has a value of D=2 for ideal smooth surfaces. By comparison, roughness factor values of real surface are between $2 \leq D \leq 3$. Applying the values of lg V as ordinate and lg (lg p_o/p) as the abscissa in the range limits of the relative pressure between $0 \leq p_o/p \leq 0.4$ supplies straight line by mean of linear regression that corresponds rise of characteristic value (s). The calculation of D is based on Equation 3.10.

$$D=3+s \tag{3.10}$$

A correction is applied to Equation 3.8 for taking into account the fractal dimension and adjustment of the real surface shape of particles.

$$d_{BET} = \left(\frac{D}{2}\right) \cdot \frac{6}{a_s \cdot \rho} \tag{3.11}$$

The specific surface (S_{BET}) of WC and Co powders are determined by BET analysis. The mean particle size ($\bar{d}_{Par}$) of each powder was calculated though by Equation 3.8. The corrected particle size ($\bar{d}_{Par,corr}$) was calculated by Equation 3.11. This value is used as the output particle size.

3.4 Density Determination of Sintered Samples

The density of the samples was determined by hydrostatic weighing by the aid of Archimede’s principle (Figure 3.10). According to ISO 3369 calculation of the sample density is achieved by measuring the mass of sample in air (m_1) and in water (m_2) [68].

$$\rho_{WC-Co} = \frac{m_1}{m_1 - m_2} \cdot \rho_{Water} \tag{3.12}$$

Additionally, the relative density, the ratio of the achieved sample density to theoretical density of the WC-Co, is characterized by Equation (3.13).

$$\rho_{rel} = \frac{\rho_{WC-Co}}{\rho_{th}} \tag{3.13}$$

Figure 3.10 Density scale, TU BA Freiberg

3.5 SEM Analysis

The structural analysis of the samples was performed on a scanning electron microscope (LEO 1530, Carl Zeiss) (Figure 3.11). The SEM investigation is a typical step after the cutting and preparation process of the sintered samples. Prior condition for WC-Co hard metal samples is demagnetization. Microstructure properties can be compared and examined by SEM micrographs.

Figure 3.11 SEM, TU BA Freiberg

Back-scattered electrons (BSE) are beam electrons that are reflected from the sample by elastic scattering. BSE images can provide information about the distribution of different elements in the sample (Figure 3.12). The BSE contrast images reflect the atomic number contrast. It seems likely that these areas are a phase of WC (light gray areas) and Co (black areas). In the most common or standard detection mode, secondary electron imaging or SEI, the SEM can produce very high-resolution images of a sample surface, revealing details less than 1 nm in size. Due to the high topographical resolution in the SE contrast image, it is possible to determine pore distribution [69].

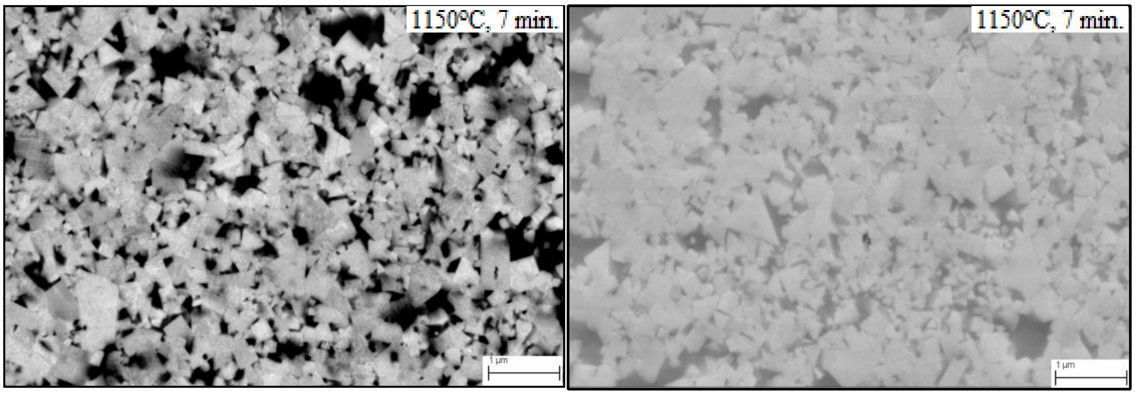

(a) (b)

Figure 3.12 (a) BSE contrast (b) SE contrast

According to ISO 4499-2, size of the WC grains could estimate subject to the BSE contrast (x100.000). For this purpose “Aquinto a4i-Analysis” image analysis program was used. About 300 grains could be measured with the help of three BSE contrast images. However from this microstructure, porosity and the grain boundry could not be detected and determined clearly. The grain size measurement uncertainty because of the intercept method is about 10% [7]. All grain boundaries can not be detected by this method.

The calculation of contiguity can be realized using Equation (3.14). The mean free path of Co (λ_{Co}) can be calculated based on Equation 3.15 with the parameters C, d_{WC} and V_{Co} (Equation 3.16).

$$\lambda_{Co} = \frac{d_{WC} \cdot V_{Co}}{(1-C)\cdot(1-V_{Co})} \tag{3.14}$$

$$C = \frac{N_{WC} - N_{Co}}{N_{WC}} \tag{3.15}$$

$$V_{Co} = \frac{L_{Co}}{L_{Co} + L_{WC}} = \frac{m_{Co}/\rho_{Co}}{m_{HM}/\rho_{HM}} = \frac{x_{Co}\cdot\rho_{HM}}{\rho_{Co}} \tag{3.16}$$

3.6 Determination of Hardness and Fracture Toughness

Hardness tests were applied to grinded, polished and embedded samples according to ISO 3878 and ISO 6507-1 by Vickers Brinell Hardness device (WPM Leipzig Ltd.) [70], [71] (Figure 3.13).

Figure 3.13 Vickers Brinell hardness device, TU BA Freiberg

Test loading is applied between 10 to 15 seconds to samples through a 136^o pyramidal diamond indenter. The Figure (3.14) illustrates schematically a Vickers hardness indentation and required parameters for determination of K_{Ic} or HV30. Three hardness indentations were introduced for each sample.

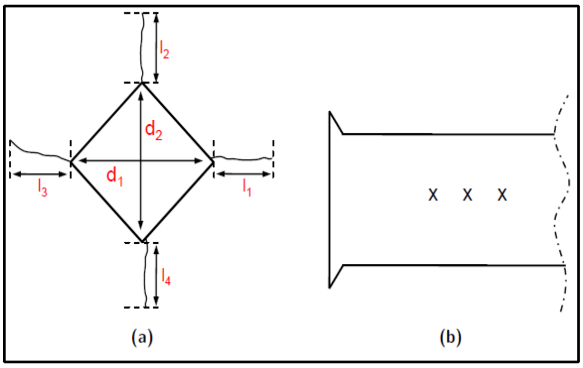

Figure 3.14 (a) Schematic representation of a Vickers hardness indentation to determine the hardness and fracture toughness and (b) distribution of hardness indentations on the sample [9]

The evaluation of the indentations was done on the light microscope (Neophot 30/200x). The Figure 3.15 shows an example of Vickers hardness indentation. The hardness can be calculated by Equation 3.17 through arithmetic mean of two diagonal (d_1 and d_2) of the indentation and the applied load.

$$HV = 0.102 \cdot \frac{2 \cdot F \cdot \frac{136^o}{2}}{d^2} \approx 0.1891 \cdot \frac{F}{d^2} \qquad (3.17)$$

The test load for HV30 is F= 294.2 N and the length of the diagonals in each case is measured in millimeter. Figure 3.14 and 3.15 show crack that is occured by hardness indentation. The sum of the length of these cracks (l_i) can be used determination of fracture thoughness for brittle materials. Equation 3.18 shows the calculation of K_{Ic}.

$$K_{Ic} = 0.0889 \cdot \sqrt{\frac{HV \cdot 30 \cdot (9.81)^2}{\Sigma l_i}} \tag{3.18}$$

If the units of HV30 and l_i are kp/mm^2 and mm respectively, the unit of K_{Ic} is MPa√m.

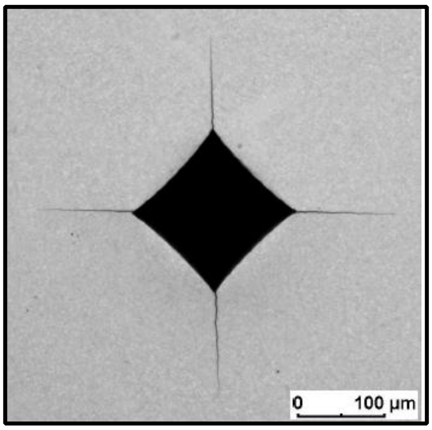

Figure 3.15 Vickers hardness indentation

3.7 Strength Behaviour

Static strength behaviour

The investigation of the static strength behavior was carried out on universal test machine “MTS 810” (Figure 3.16).

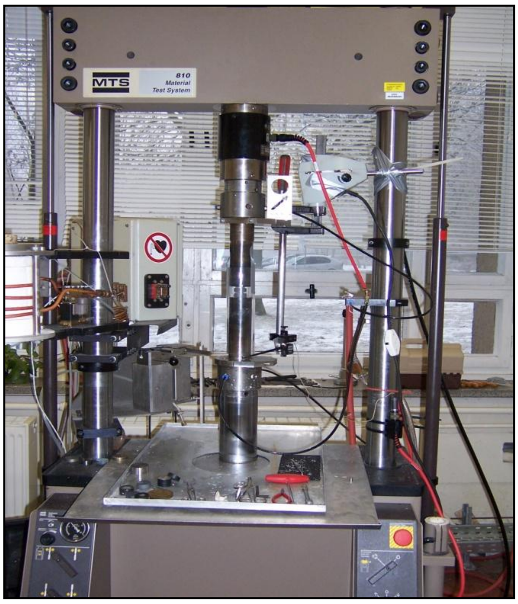

Figure 3.16 Compression test machine, TU BA Freiberg

According to ISO 4506, the ratio between the height and diameter of samples should be approximately one (ho/do~1) [72]. The elastic strain rate during compression tests was about $\dot{\varepsilon} = 10^{-4} s^{-1}$. Piston speed was calculated by Equation 3.19.

$$\upsilon_{\text{Piston}} \approx h_o \cdot \dot{\varepsilon} \tag{3.19}$$

Figure 3.17 shows schematically sample, machine stamp and hard metal pressure disks.

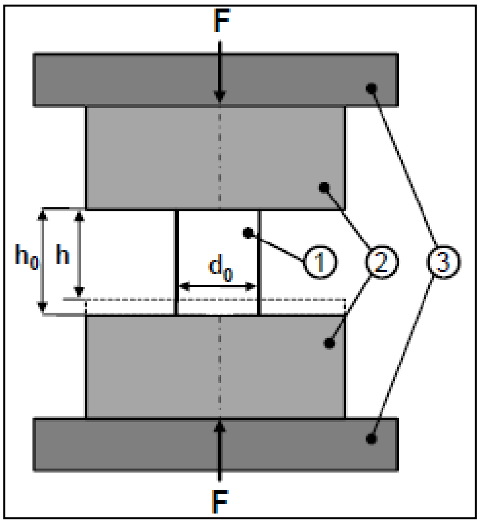

Figure 3.17 Schematically design of static compressive test 1) sample 2) hard metal disks 3) machine stamp [9]

The measurement of the piston travel for process control was carried out with an inductive displacement sensor in the machine. In addition, the continuously increasing force due to the axial compressive stress was measured with a load cell.

The compressive stress of sample during the test can be calculated by following equations.

$$\sigma_c = \frac{F}{A_o} = \frac{4 \cdot F}{\pi \cdot d_o^{\,2}} \tag{3.20}$$

The compressive strength depends on maximum force and surface area of sample (Equation 3.21).

$$\sigma_{cs} = \frac{F\max}{A_o} = \frac{4 \cdot F\max}{\pi \cdot d_o^{\,2}} \tag{3.21}$$

Dynamic Strength

The dynamic compression test at high loading rates were performed on a drop weight testing machine (Figure 3.18). During the tests same sample dimensions were used as in static compression tests. With the aid of grease the positioning of the sample was adjusted on a hard metal. In addition a hard metal was fixed to punch. The material of punch is maraging steel. During the experiment, the weight and height of drop were about 180 kg and 50 mm respectively. So that the elastic strain rate was $\dot{\varepsilon} = 5 \cdot 10^1 s^{-1}$.

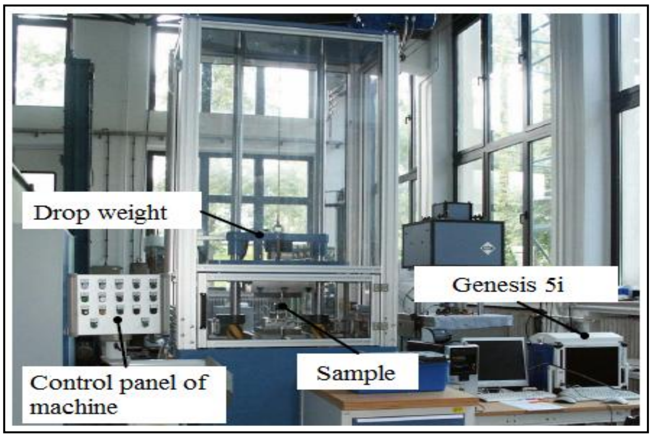

Figure 3.18 Drop weight testing machine, TU BA Freiberg

A Kuebler measuring system of 10 µm is used to register displacement changes. Force measurement due to the elastic deformation of the punch was determined with the help of strain gauges which were fixed on the punch. A static calibration factor (m) were used during the measurement of force. The static calibration factor that was derived from slope of the curve force-voltage, the amplification factor (A_F) and the bridge voltage (V_g) were 143.258 (kN/V), 200 and 2.5 V, respectively.

The applied force during the dynamic compression test can be calculated by Equation 3.22 due to measured voltage (V).

$$F = m \cdot V \tag{3.22}$$

These measured data were collected in the data acquisition system “Genesis 5i” and were evaluated by the program “IMC FAMOS”.

Split Hopkinson Pressure Bar Test

The name of a characterization tool for the mechanical reaction of materials at high strain rates (10^2 – 10^4 s^{-1}) is a Kolsky bar, in other saying Hopkinson pressure bar (SHPB) [73].

It is shown that a sample is sandwiched between an elastic incident and a transmitted bar in a compression split-Hopkinson pressure bar in Figure 3.19.

The stress and strain cases at each end of the sample can be determined by the elastic displacements in the incident and transmitted bar.

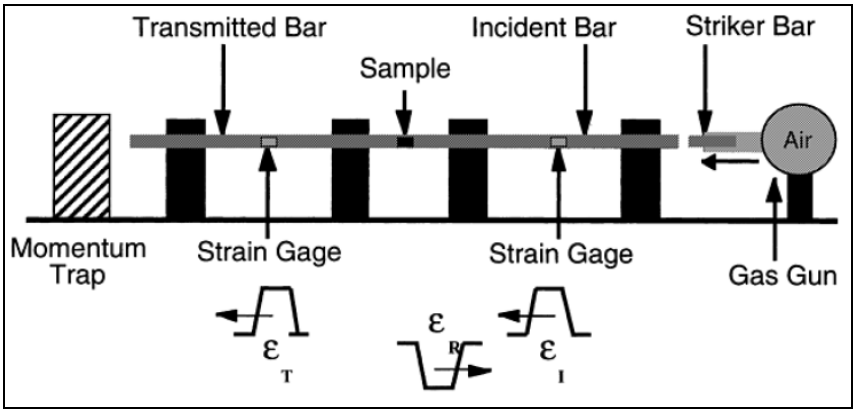

Figure 3.19 Schematic of a compression split-Hopkinson pressure bar [73]

According to elastic relations (Equation 3.23 and 3.24), one can calculate the stresses at the both ends of the specimen,

$$\sigma_1 = \frac{A_B}{A_S} \cdot E_B(\varepsilon_I + \varepsilon_R) \tag{3.23}$$

$$\sigma_2 = \frac{A_B}{A_S} \cdot E_B \cdot \varepsilon_T \tag{3.24}$$

where A_B and As are the cross-sectional areas of the bars and the specimen, the subscripts, I , R , and T , symbolize the incident, reflected, and transmitted pulses respectively; and E_B is Young's modulus of the bar material.

In a Kolsky-bar experiment, there is an assumption that the stress which has an effect on specimen is equilibrated and this correlation is effective in dynamic characterization of material properties.

The stress equilibration is explained as,

$$\sigma_1 = \sigma_2 \tag{3.25}$$

The above stated equations are used in engineering measurements and the values are positive in compression. One can calculate the average value of the stresses at both sample ends as the sample stres is not in explicit equilibrium,

$$\sigma = \frac{1}{2}(\sigma_1 + \sigma_2) = \frac{1}{2} \cdot \frac{A_B}{A_S} \cdot E_B(\varepsilon_I + \varepsilon_R + \varepsilon_T) \tag{3.26}$$

A average specimen stress is obtained by this method. Equation (3.26) is not used for stress measurement if the stres or strain in the specimen is in a certain multiplicity. The specimen stress and strain conditions should be qualified. Then, stress-strain relationship is determined by eliminating the time variable [74].

Because of the special structure of SHPB (Figure 3.20) accurate strain of sample was realized in contrast to drop weight test. The level of the strain rate and load can be regulated via the charging pressure of the SHPB and the striker length. In the SHPB the projectile was shot to the incident bar via compressed air. Thereby by means of a pulse shaper, the shape of the shock pulse can be changed. So that the increasing of the pulse are flattened to the maximum and constant strain rate and a stress balance is generated in the sample. The pulse shaper consists of a small copper plate and a piece of rubber and both of them were attached with a little grease on the front side of incident bar.

Figure 3.20 SHPB apparatus, TU BA Freiberg

In standart tests, the sample is positioned between the incident bar and transmission bar. Since the sample for each test should be loaded only once. In front and behind of the sample two impedance matching hard metal disks were fixed to protect indentation of the sample into the bars. The connection of the bars were greased for better wave transmission.

The strength behaviour of sample 974 was performed with the Split Hopkinson Pressure Bar test, too. The bars of SHPB were made of maraging steel (E=191.6 GPa). The length of striker, incident and transmission bar is 194, 1847 and 930 mm, respectively. In front and behind of the sample hard metal disks (d=12.3 mm and h=12.15 mm) were used in order to prevent impedance jumps. The diameter and thickness of pulse shaper were 2.9 mm and 0.75 mm, respectively. The strain of sample was determined by means of wave analysis and thereby there are three variants. The one wave analysis uses only the transmitted pulses, the 2-wave analysis uses the incident and reflected pulses from the incident bar. All three strain signals are used for evaluation in the 3-wave analysis.

3.8 Determination of Elastic Modulus via the Ultrasonic Test Method

The ultrasound waves can be used to measure elastic modulus (Figure 3.21). A piezoelectric transducer compose transverse and longitudinal waves in the sample. The pulse-echo method where transducer acts as transmitter and receiver of the sound pulse was used on experiments. At the measurements, a longitudinal focusing probe “V110” and a focusing transverse probe “V156” was used. Also a coupling agent was used. The longitudinal sound wave velocity (v_l) and transversal sound wave velocity (v_t) can be calculated by quotitent of the path (double specimen height) and the time between the second and third bottom echo.

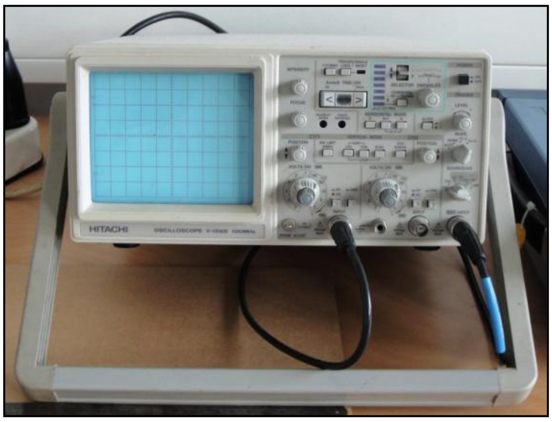

Figure 3.21 HITACHI Oscilloscope V-1565 100 MHz, TU BA Freiberg

According to EN 843-2, Equation (3.27) shows the calculation of the elastic modulus [75].

$$E_{US} = \rho_{HM} \frac{3\nu_l^2 \nu_t^2 - 4\nu_t^4}{\nu_l^2 - \nu_t^2} \tag{3.27}$$

Poisson’s ratio can be calculated as follows:

$$\nu = \frac{1}{2} \frac{\upsilon_l^2 - 2\upsilon_t^2}{\upsilon_l^2 - \upsilon_t^2} \tag{3.28}$$

CHAPTER 4

RESULTS AND DISCUSSION

Figure 4.1 shows the SEM micrographs of the WC powder (WC (DN 4-0)) and Co-HMP powder.

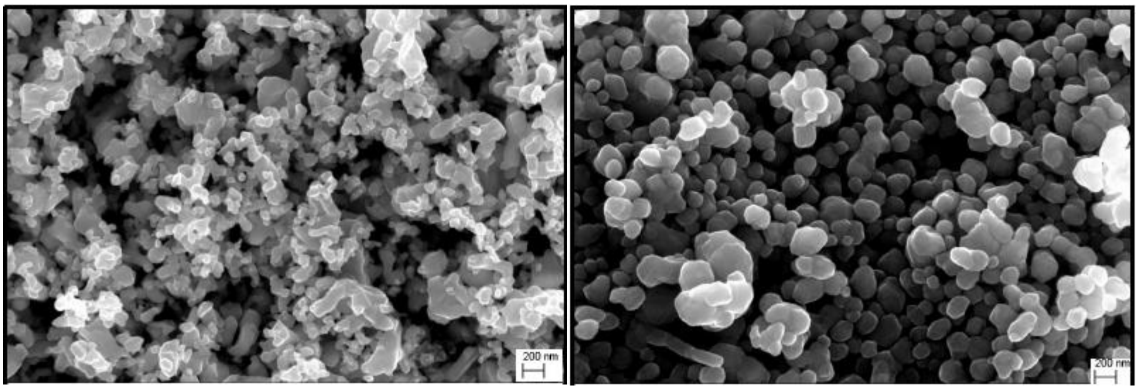

(a) SEM image of WC (DN 4-0) powder (b) SEM image of Co powder

Figure 4.1 SEM images of WC and Co powders

As it can be seen in Figure 4.1, when the Co powder approximately spherical, the WC powder shows agglomeration. This can effect the milling conditions, Co distrubition and thus the mechanical properties of sintered samples.

The selected paramaters in milling based on experience that a variation of milling time. The aim is mixing of WC and Co powders, not to reducing the particle size of raw materials. For this purpose, increasing milling time was applied. The Figure 4.2 shows the particle size distribution of WC-12Co powder after different milling times. The table 4.1 shows the results of BET analysis and grain size for the WC-12Co powder.

Table 4.1 shows that when the milling time increases, the specific surface area increases due to decreasing of grain size. Therefore much more energy is required to activation of new surface area.

Table 4.1 Specific surface area and grain size of WC-12Co powder

Powder	**S_{BET} [m^2/g]**	**$\bar{d}_{Par.corr}$[nm]**	**$\bar{d}_{Matlab}$[nm]**
WC-12Co_{500}	3.932	118.721	119.19
WC-12Co_{1000}	4.197	116.624	112.45
WC-12Co_{1500}	4.687	106.062	108.29

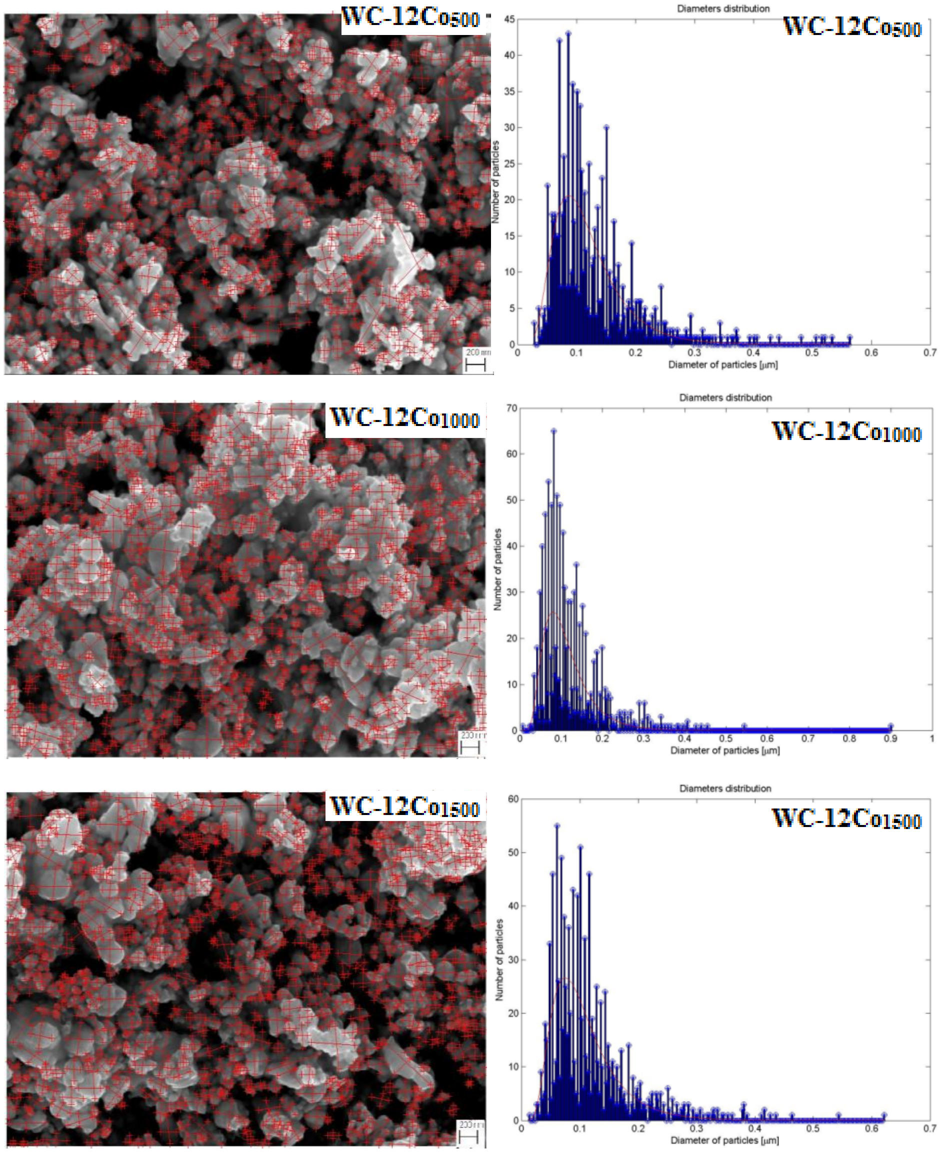

Figure 4.2 Matlab-Skript of WC-12Co powder

4.1 Influence of Production Procedure

Porosity can take place due to flowing of molten Co during the sintering process. On the other hand, there is also the possibility that the Co can be diffused the graphite foil during the sintering process. The solubility of WC in Co increases with decreasing of WC grain size. The amount of WC solution within the binder phase can be based on the magnetic saturation. In addition a distortion of the lattice parameters relevant to the compressive residual stresses in the WC phase and tensile stresses in the Co phase due to the different thermal expansion coefficient. These factors influence the density of WC and Co and the theoretical density of the each sintered sample.

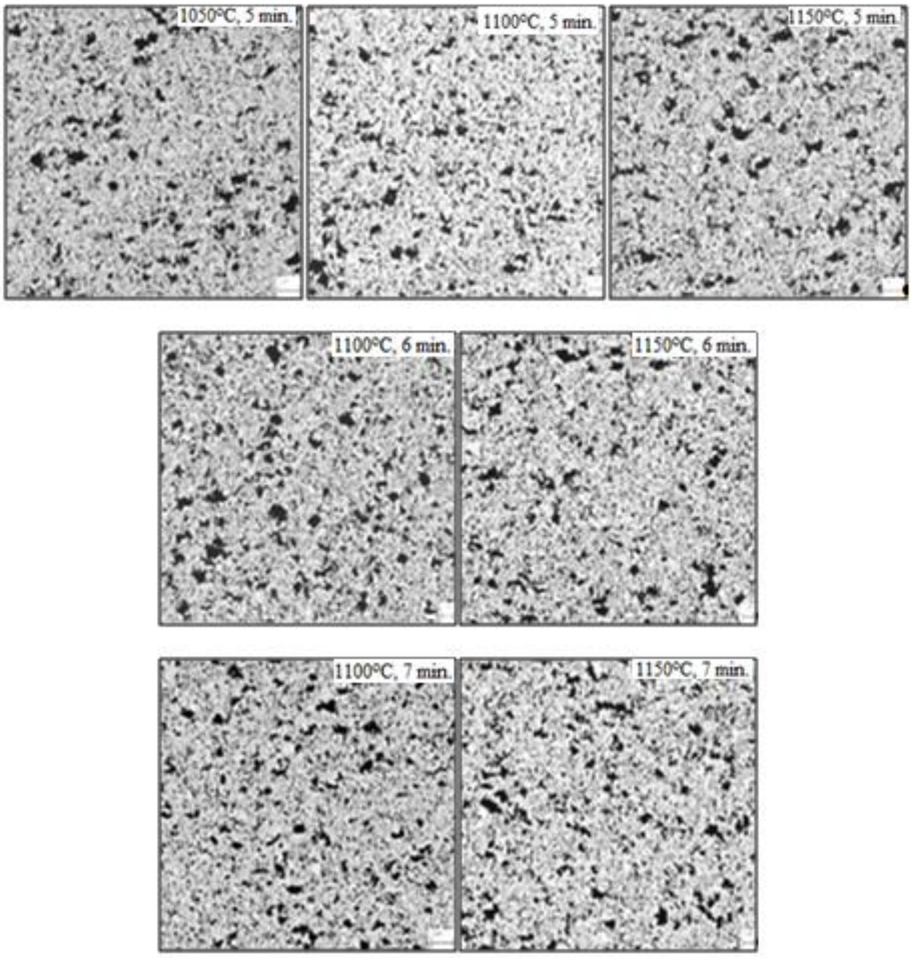

Figure 4.3 SEM image of the samples

As is seen from the SEM images of these samples Figure (4.3), the η-phase $x_{Co_3W_3C}$ is not detected [76]. The $x_{Co_3W_3C}$ phase has a cubic structure with cyrstal space group Fd3m. By the occurence of this phase, the proportion of binder phase reduces and brittleness of the material rises because of η-phase is very brittle. The formation of η-phase is associated directly proportional with decarburization [77]. The waiting time of powder until the sintering process effect this insignificantly. Independently of manufacturing routine (milling and sintering parameters), the η-phase were not detected at sintered samples because powder preparation and sintering process are realized under inert gas atmosphere and vacuum, respectively.

Table 4.2 shows the relative density of samples. Small deviations can cause to major errors in the composition of the sintered samples. W and C dissolve in the Co phase during the sintering process. So that, the stabilization of Co (fcc Co) at high temperature modification is achieved in the sintered sample.

Table 4.2 Relative density of samples

Sample Number	**T_{Sinter} [^oC]**	**Density [g/cm^3]**	**Relative density [%]**
919	1150	14.20	99.1
921	1150	14.17	98.9
941	1150	14.21	99.2
942	1150	14.17	98.9
943	1100	14.20	99.1
946	1100	14.17	98.9
947	1100	14.20	99.1
966	1150	14.22	99.3
967	1050	14.22	99.3
974	1050	14.19	99.0
975	1050	14.20	99.1

The milling process has an important influence on the powder particle size and the mixing of WC and Co. In this chapter the effect of milling on the Co-distribution on the hard metal samples is investigated. The investigation of the Co distribution was carried out on the SEM images of sample 895 (500 min milling time), 919 (1000 min milling time) and 921 (1500 min milling time). For this purpose, a BSE contrast image from the core region of the sample at 30.000 times magnifiction was chosen (Figure 4.4).

A heterogene Co distribuition tends to increase with increasing milling time. Although samples were sintered under same conditions, the SEM images of samples are considerably different. Sample 895 shows homogeneous Co distrubition. In general, this may be attributable to the standing time of the powder but all the samples were sieved before the sintering process. In this case, the Co distribution can not be attributed the segregation of the powder. Even tough the milling time is 1500 min, there are regions where the contiguity of WC grains is large. This leads to the assumption that more homogeneous Co distribution can be achieved by milling time of 500 min.

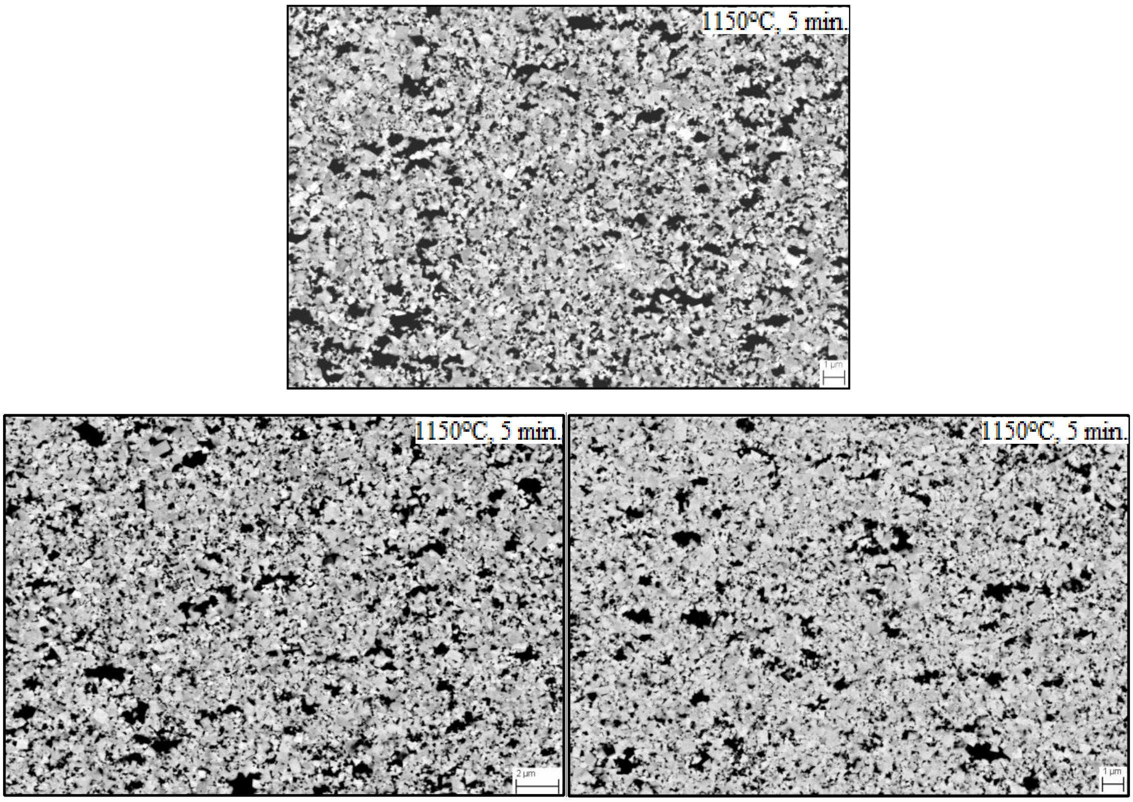

Figure 4.4 SEM image of 895, 919 and 921

So that, the increasing of milling time considerably has not an influence on Co distrubition. Both milling time 1000 min and 1500 min could not be achieved homogeneous Co distribution. As a result, this causes the Co agglomeration during sintering and a gradient of mechanical properties. Also, low Co concentration causes increasing of hardness while the toughness is decreasing. The higher contiguity owing to low Co distribution increases the amount of WC-WC grain boundary. When a compressive stress is applied, a crack propagation probably occurs on these areas. An inhomogeneous Co distrubition can cause premature failure, too.

A variation of the parameters can be choiced, such as reducing the number of rotation or the changing of BPR to obtain homogeneous distribution. The reduction of C and λ_{Co} can be achieved by a homogenous Co distribution.

4.2 Variation of the Sintering Parameters

The Figure 4.5 is representing sinter curves of sample 967, 946 and 942 with a sintering time of 5, 6 and 7 min at 1050, 1100 and 1150 ^{o}C, respectively. The precompression was applied to all samples. Therefore identical compressive force curve was selected for all samples. So that, the maximum pressure is 79.6 MPa during sintering temperature.

Figure 4.5 illustrates that beginning of T_{sinter} is same for all samples. Until the reaching degassification zone (t=7 min), the piston travel (Δx_{piston}) is same for every samples. The small differences are resulted from the different amount of powder in tool and the fluctuation of precompression outside of SPS.

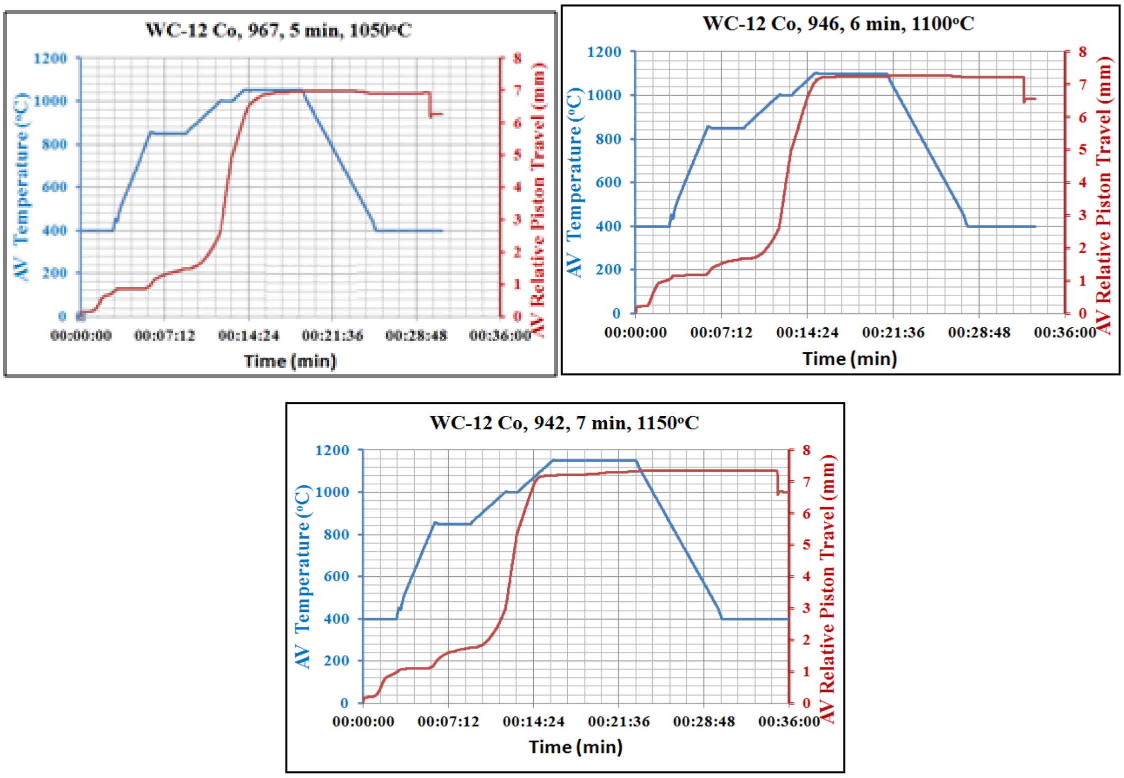

Figure 4.5 Variation of sintering parameters

Also during the degassing phase (T=850^{o}C) takes place a progressive compaction of the sample. This can be seen by the increase of piston travel. Between t=9 min and t=10, the Δx_{piston}-t_{min} curve is almost parallel to the abcissa. This shows that at T=850^{o}C, the maximum precompression (F=8 kN) can be achieved. The biggest compression rate was performed during the sintering temperature (T_{sinter}) and the force reaches to 25 kN in 1 minutes at 1000 ^{o}C. The nearly horizantal curve in Figure 4.5 can be explained force withdrawal during lowly shrinkage of the sample due to controlled cooling.

Influence of sintering time

Based on experience, the sintering process was carried out between t_{sinter}=5 min and t_{sinter}=7 min to determine the effects of sintering time. The Figure 4.6 shows the comparison of the relative density.

Although the same preparation routine was used, the relative density of sample 943 (T_{sinter} = 1100 ^oC, t_{sinter} = 5 min) and 947 (T_{sinter} = 1100 ^oC, t_{sinter} = 7 min) are 99.1%. On the one hand, the influence of sintering time on the WC grain size is inefficient (Figure 4.7). This can be explained by the almost linear correlation of grain growth with time and the exponential correlation of grain growth with the temperature [78]. Also, the effect of sintering time on C and λ_{Co} is not significant according to Figure 4.8 and 4.9.

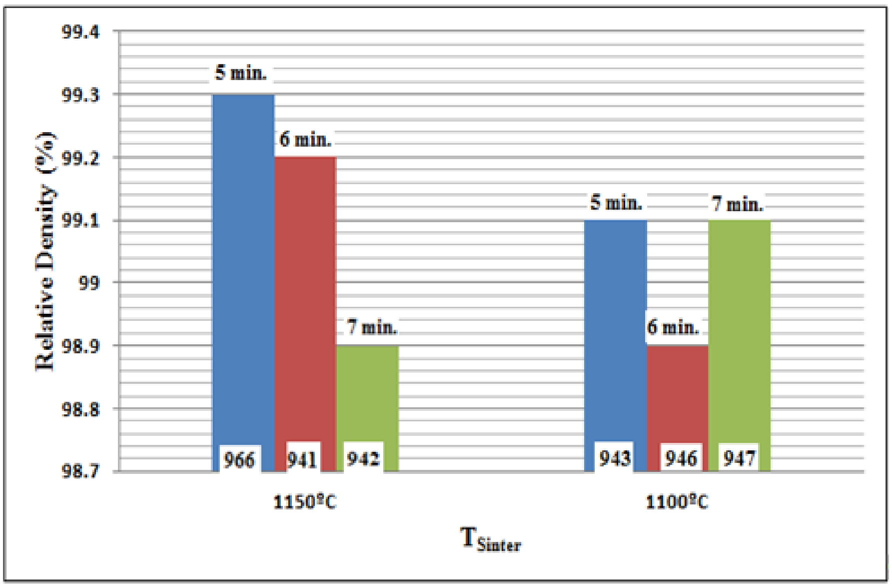

Figure 4.6 Comparison of density (Cooling rate = 100 K/min)

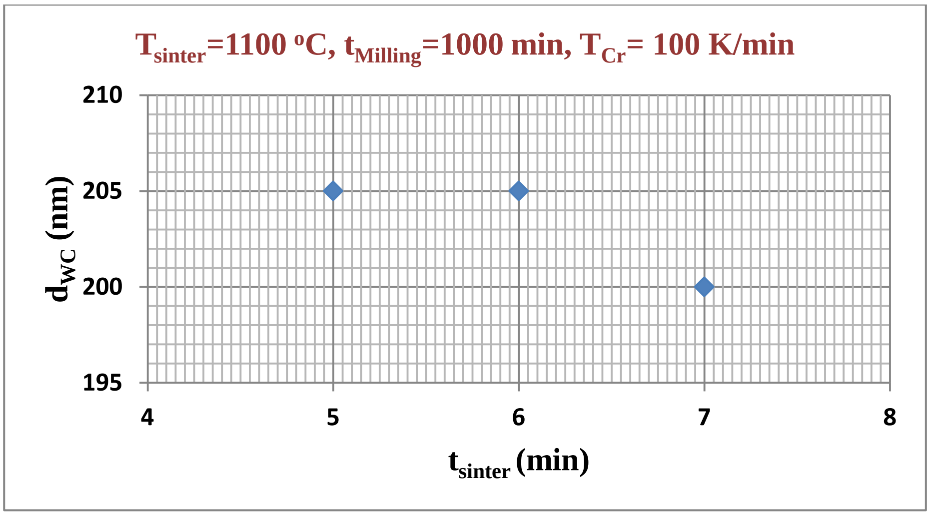

Figure 4.7 Relation between sintering time and WC grain size

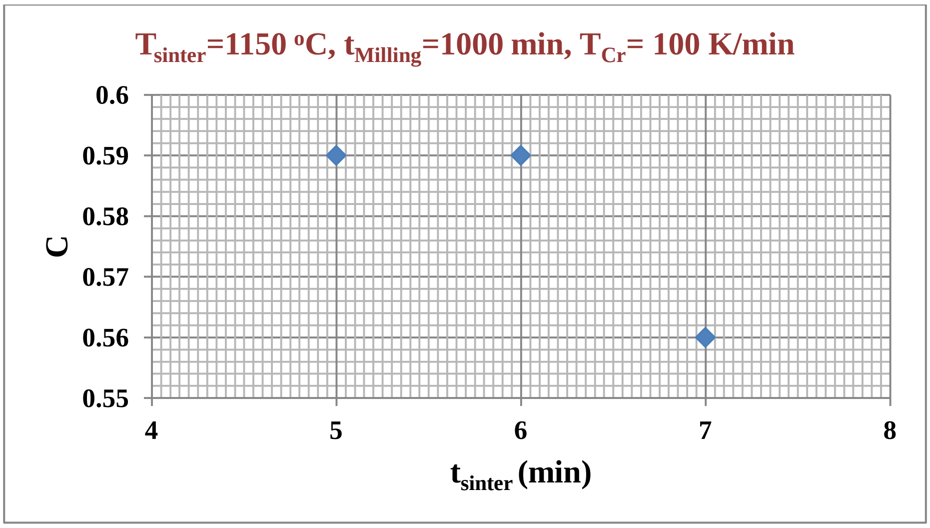

Figure 4.8 Correlation between contiguity of WC phase and sintering time

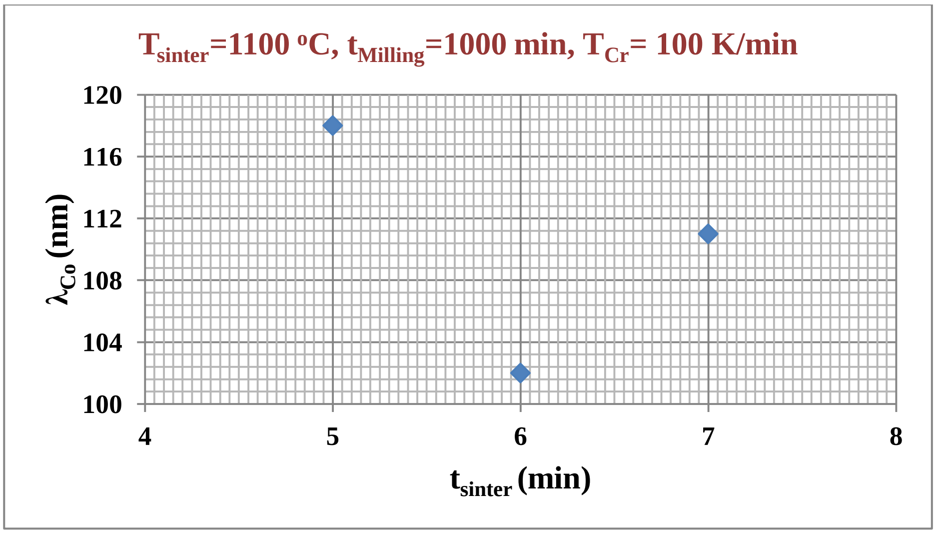

Figure 4.9 Changing of mean free path of the Co phase owing to the sintering time

Influence of sintering temperature

The sintering temperature was varied between 1050 ^{o}C and 1150 ^{o}C for the samples. Figure 4.10 illustrates the dependence of the relative density to sintering temperature. It is seen that, the correlation between relative density and sintering temperature can not clearly be determined by results of sintered samples. The relative density of both sample 966 and 967 are 99.3 %. The deviation of the relative density values is about ± 0.2 % that is acceptable.

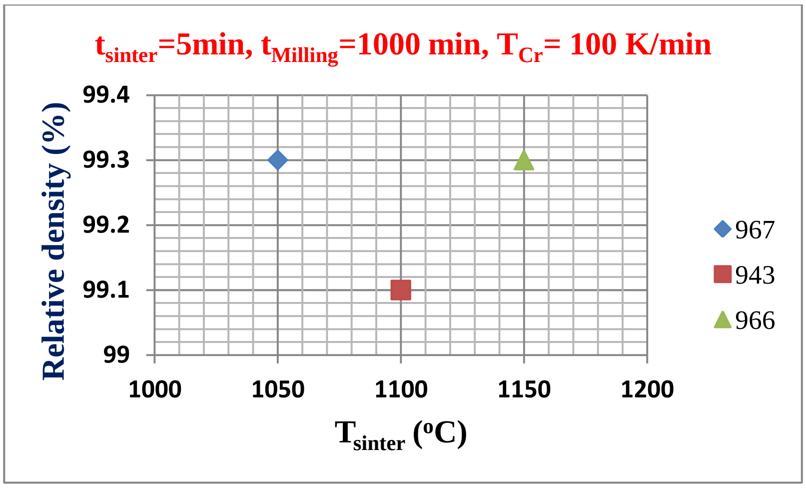

Figure 4.10 Changing of relative density due to the sintering temperature

In accordance with literature reviews, the grain size of samples increased slowly with incresing sintering temperature during solid state sintering. As it is seen in Figure 4.11, there is not a significant grain growth. On the one hand, higher sintering temperature affects C and λ_{Co} values (Figure 4.12 and 4.13). The deformation behaviour of WC-Co cemented carbides impresses with larger contiguity of WC phase and higher mean free path of Co phase. This can cause microcracks while plastic deformation.

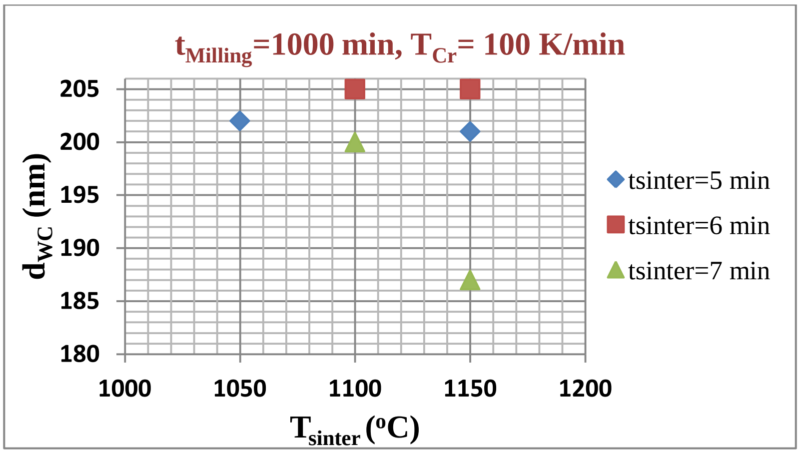

Figure 4.11 Influence of sintering temperature on the WC grain size

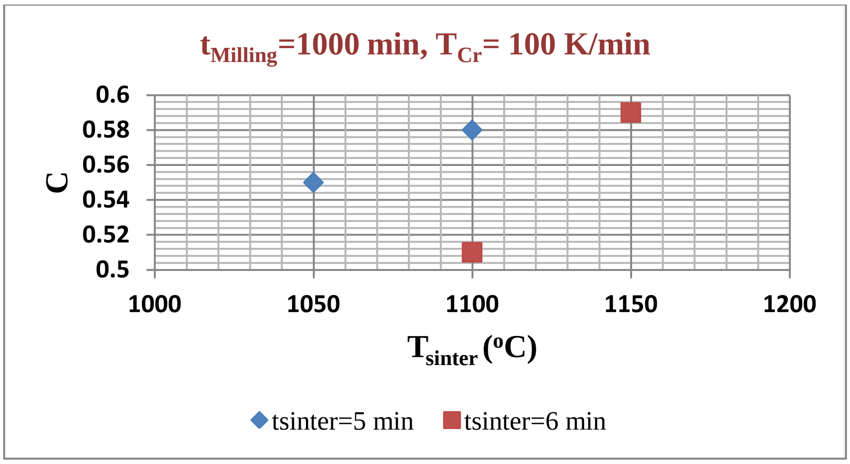

Figure 4.12 Effect of sintering temperature on contiguity of the WC phase

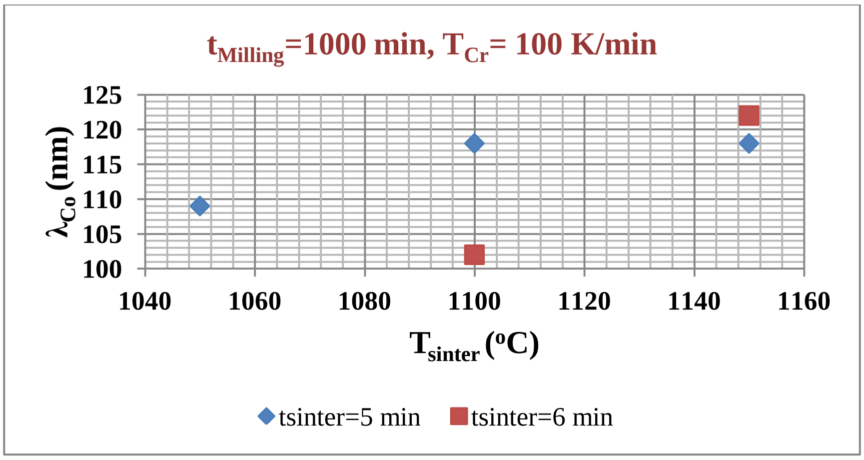

Figure 4.13 Changing of mean free path of the Co phase owing to the sintering time

Influence of cooling rate

Table 4.3 shows the structural parameters and mechanical characteristics of the samples 967, 974 and 975. The density and microstructure parameters such as d_{wc}, λ_{co} and C are illustrated comparability of the samples 967, 974 and 975.

Table 4.3 Influence of cooling rate

Sample Number	$\dot{T}_{Cool}$ [K/min]	ρ_{rel} [%]	d_{WC} [nm]	λ_{Co} [nm]	C	Hardness [HV 30]	K_{Ic} [$MPa\sqrt{m}$]
967	100	99.3	202	109	0.55	1818	10.1
975	150	99.1	197	118	0.60	1773	10.6
974	200	99.0	176	112	0.62	1800	10.2

One can see the deviations of the fracture toughness. According to literature researches the fracture toughness increases by slow and controlled cooling process and the different thermal expansion of WC and Co cause residual tensile stresses that can be reduced with lower temperature gradient and diffusion process. There is not a correlation between literature review and the experimental results. Although grain growth was occured by slow cooling, the reduction of hardness was not observed due to a higher relative density value.

4.3 Mechanical Properties

The best mechanical properties that depend on microstructure were achieved by optimum temperature range (Sample 967). At higher temperatures Co can diffuse faster. This leads to the formation of narrow binding phase regions between the WC grains that cause reduction of Co clusters and porosity (Sample 941, λ_{Co} = 122 nm, C = 122). So that higher hardness values were obtained. Simultaneously there is an insignificant improving of fracture toughness values despite reduction of λ_{Co} that is probably the result of energy dissipation due to crack branching or crack deflection. The measured hardness and fracture toughness values prove results of the SEM investigations. Figure 4.14 shows the correlation between hardness and relative density of WC-12Co samples.

4.3.1 Hardness and fracture toughness

Hardness tends to rise due to increasing of relative density. As a result of much porosity, the Vickers pyramid can penetrate deeper into the material that cause enlargement of the indentation diagonal hence the decreasing of resistance to penetration of Vickers pyramid. According to hardness equation, lower hardness values are determined.

A decrease in strength can combine with existing porosity. In view of the fracture toughness, there is not a correlation with sample density. The porosity adversely effects Co distrubition.

Consequently, the plastic deformation of the ductile binder phase can delay the cracks. The decrease of fracture toughness can be explained by notch effects of sinter neck between the particles. Pores can positively affect the fracture toughness because of pores can round of the crack tip when a crack runs into a pore. Furthermore, a energy dissapiation can occur due to crack branching. Table 4.4 illustrates fracture toughness and hardness values of the samples.

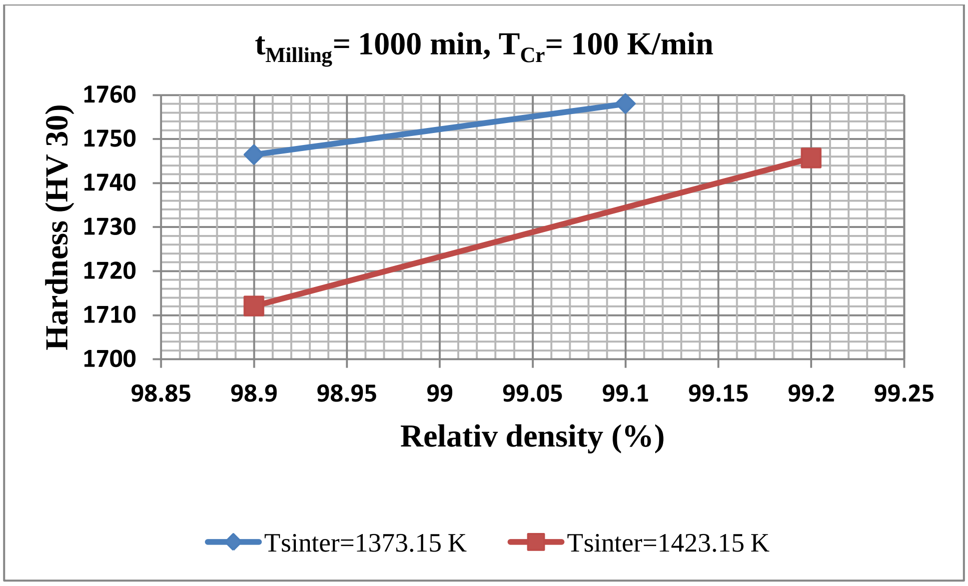

Figure 4.14 Correlation between relative density and hardness

Table 4.4 Fracture toughness and hardness of the samples

Sample Number	$t_{Milling}$(min)	T_{Sinter}[^oC]	t_{Sinter}[min]	$\dot{T}_{Cool}$ [K/min]	HV30	K_{Ic} [MPa√m]
919	1000	1150	5	93.3	1608	10.5
921	1500	1150	5	93.3	1674	10.56
941	1000	1150	6	100	1746	10.37
942	1000	1150	7	100	1712	10.2
943	1000	1100	5	100	1758	9.93
946	1000	1100	6	100	1746	10.18
947	1000	1100	7	100	1746	10.31
966	1000	1150	5	100	1732	10.19
967	1000	1050	5	100	1818	10.11
974	1000	1050	5	200	1800	10.24
975	1000	1050	5	150	1773	10.6

Figure 4.15 shows the correlation between hardness and fracture toughness. The fracture toughness of nanocrystalline WC-Co hard metals depend on hardness inversely.

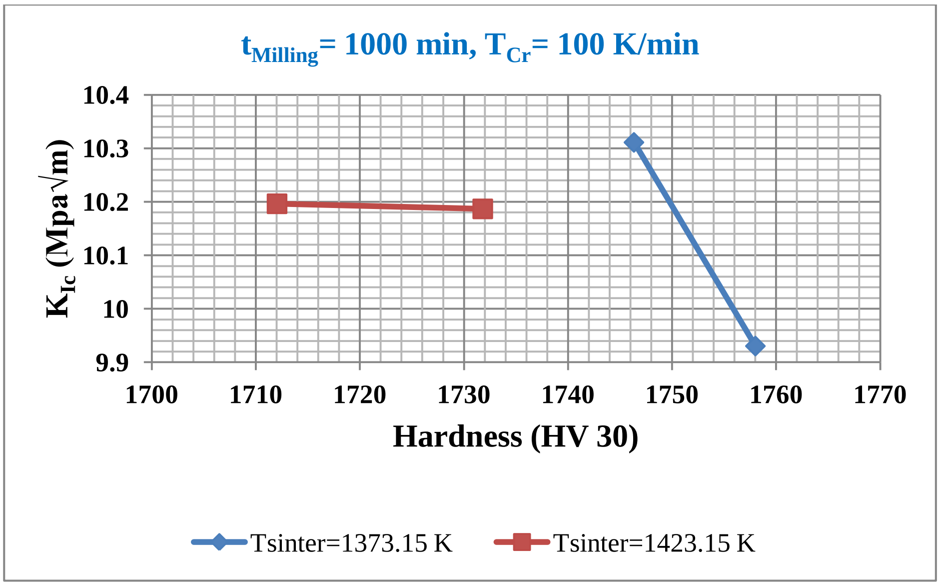

Figure 4.15 Correlation between hardness and fracture toughness

Figure 4.16 illustrates the correlation between hardness and WC grain size depending on sintering temperature. When the grain size of WC increases, the hardness value of samples increases in terms of figure. However, the investigations show that the hardness of WC-Co cemented carbides increases with the decreasing WC grain size. This situation can be explained by the higher density of the each sample. Because the WC grain size values of the samples are close. The relative density of sample 947 which were sintered at 1100 ^{o}C is 99.1% is higher than sample 942 (98.9 %). As mentioned before, the effect of sintering temperature on WC grain size is insignificant.

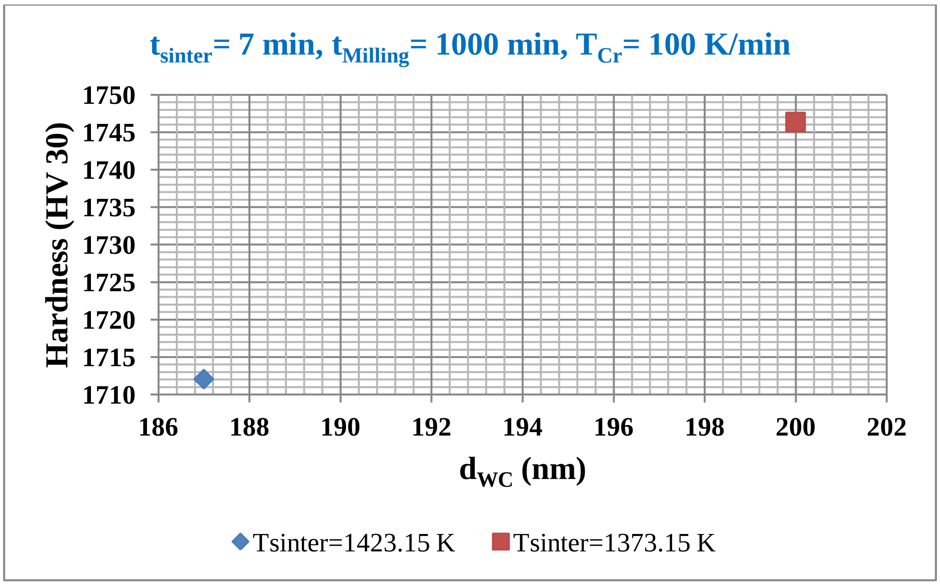

Figure 4.16 Correlation between WC grain size and hardness

A decrease in fracture toughness can be observed not only reducing of WC grain size moreover decreasing of λ_{Co}, too. This presumably causes the reduction of the plastic zone in front of the crack. Consequently, the crack growth ist restricted by plastic deformation of binder phase in front of the crack.

The binder phase regions decrease with decreasing WC grain size that can cause the saturation of hardness. This leads to reduction of ductility. So that, the crack propagation can take place easily.

Table 4.5 shows comparable values for WC-Co samples from the literature. It is clear that the literature values for hardness and fracture toughness are usually higher than the experimentally determined values. Because the literature values due to nearly complete densification (ρ_{rel} ~ 99.9%). The realization of a complete densification is one of the most important conditions to achieve good mechanical properties. The comparison of measurements with literature values is only conditionally possible. This is partly due to the deviations of density values or the composition of the sintered samples with regard to WC grain size. In addition, influencing of structure can depend on grain growth inhibitors. Furthermore, different sintering devices are used that restrain the comparison of the sintering temperatures. It is often not clear how many individual measurements are based on literature values.

Table 4.5 Literature values of hardness and fracture toughness [18], [29]

Device	**T_{sinter} [°C]**	**t_{sinter} [min]**	**P_{sinter} [MPa]**	**HR [K/min]**	**d_{WC} [nm]**	**x_{Co} [wt %]**	**Hardness**	**K_{Ic} [MPa√m]**	**Rel. Density [%]**
FCT HP D 25/1	1100	5	80	100	216	12	1830 HV30	10.5	99.94
FCT HP D 25/1	1260	2	60	200	280	12	1575 HV10	9.5	99.10
Sample 967	1050	5	80	100	202	12	1818 HV30	10.11	99.3

The evaluation of the measured values is only partially possible because of the influence of density parameters, WC grain size and Co distribution. So that, correlation between the hardness and fracture toughness can not be rated separetely. The reason of fracture toughness decrease for the sample 943 (9.93 MPa√m) is probably an inhomogeneous

Co distribution. The increasing of fracture toughness without a significant decrease in hardness is presumably based on controlled cooling.

4.3.2 Compressive strength

Table 4.6 shows the results of quasistatic compressive strength of samples due to different sintering and milling conditions.

Table 4.6 Quasistatic compressive strength of the samples

Sample Number	**$t_{Milling}$ [min]**	**T_{Sinter} [^{o}C]**	**t_{Sinter} [min]**	**$\dot{T}_{Cool}$ [K/min]**	**$\sigma_{cs, quasistatic}$ [MPa]**
919	1000	1150	5	93.3	4340±180
921	1500	1150	5	93.3	4380±180
941	1000	1150	6	100	4430±180
942	1000	1150	7	100	3920±445
943	1000	1100	5	100	3820±185
946	1000	1100	6	100	4720±690
947	1000	1100	7	100	4480±285
966	1000	1150	5	100	4520±80
967	1000	1050	5	100	5290±605
974	1000	1050	5	200	4540±100
975	1000	1050	5	150	5060±350

There is a correlation between milling time and compressive strength (Figure 4.17). Compressive strength increases together with milling time. The milling time of sample 921 and compressive strength are 1500 min and approximately 4380 MPa, respectively. On the other part the compressive strength of sample 895 is only 4070 MPa. This correlation can be explanied by decreasing of d_{part} and d_{WC} with increasing milling time.

Figure 4.18 shows the effect of cooling rate on compressive strength. As can be seen in the figure below, compressive strength decreases with increasing cooling rate. Although the measured compressive strength value of the sample 967 is 5290 MPa, it is only 4540

MPa for the sample 974. Because internal stresses increase with increasing cooling rate and the scattering of the results increases with the brittleness of the material.

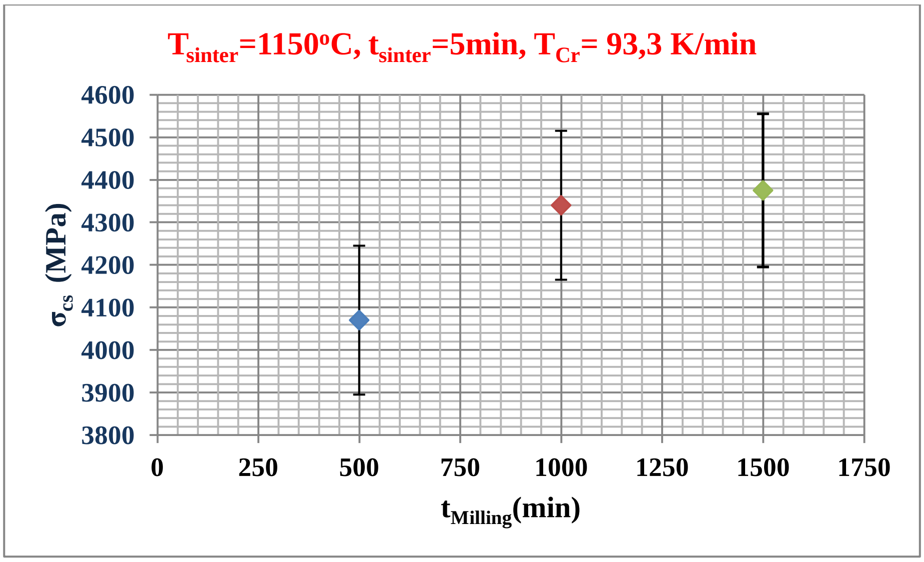

Figure 4.17 Correlation between milling time and compressive strength

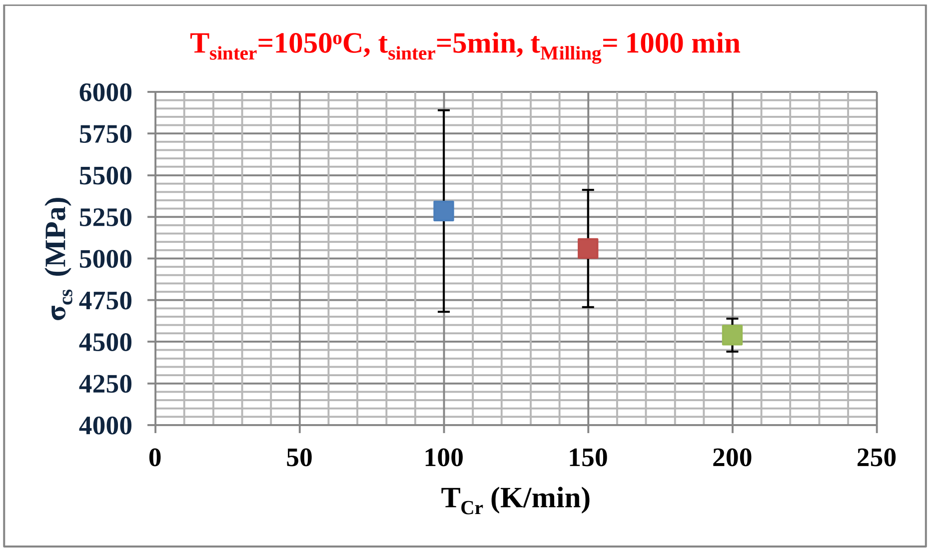

Figure 4.18 Changing of compressive strength due to cooling rate

The effect of sintering time on mechanical properties is not significant due to other test results (Figure 4.19). The differences of measured values between the sample 966 (4520 MPa) and 941 (4430 MPa) are not remerkable. On the one hand it is too low for the sample 942 (3920 MPa). Because the relative density values of these samples are 99.3%, 99.2 % and 98.9 %, respectively.

Production of cylindrical samples has an influence on the measured compressive strength. Surface defects cause premature failure and introduce different measurement values in compression test. Also slight property gradients between center and edge of the sample and can lead to deviations.

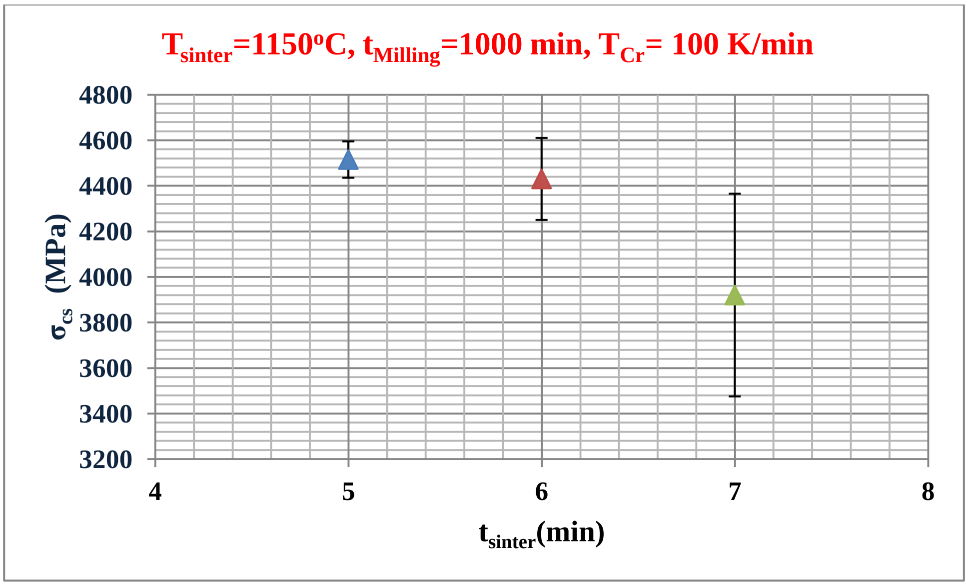

Figure 4.19 Correlation between sintering time and compressive strength

In general, a higher density provides an increase in compressive strength. As it is seen in Figure 4.20 the compressive strength decreases with increasing porosity. The determination of porosity depends on the relative density value.

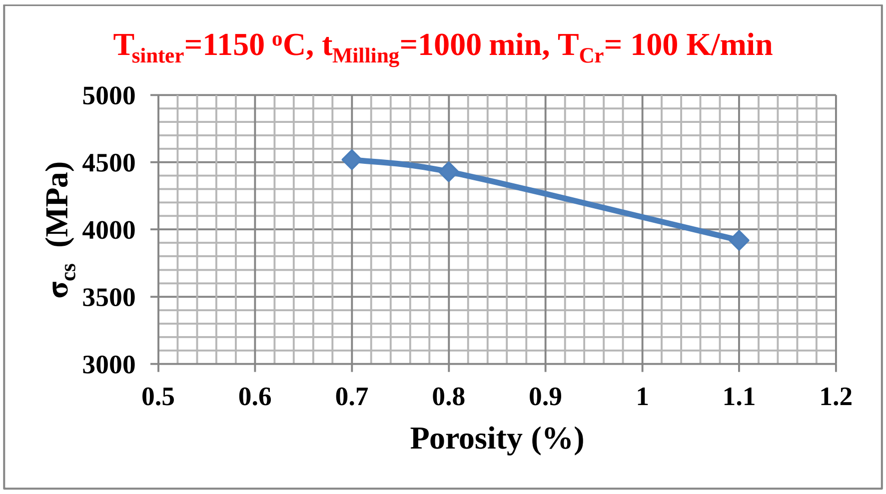

Figure 4.20 Effect of relative density on compressive strength

Deformation behaviour of WC-Co hard metals depend on structural parameters (Table 4.7). Figure 4.21 illustrates the dependency of compressive strength on sintering temperature. When the sintering temperature increases, the compressive strength decreases due to higher contiguity of WC phase and/or higher mean free path of Co phase. When the contiguity is high, the load trasmitted within the carbide phase which is brittle. On the one hand the binder phase carries more of the load and dissipates strain energy. So that, the highest compressive strength value is 5290 MPa at 1050°C (Sample 967, d_{rel} = 99.3 %).

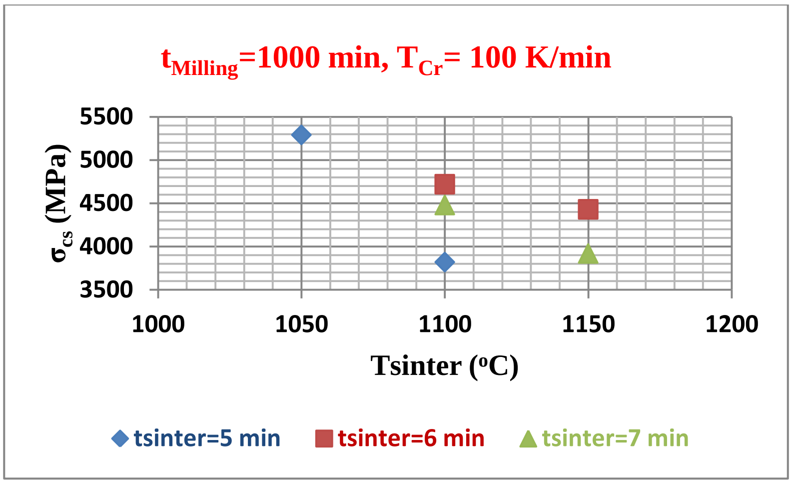

Figure 4.21 Dependency of compressive strength on sintering temperature

Table 4.7 Structural parameters of the samples

Sample Number	**T_{Sinter} [°C]**	**t_{Sinter} [min]**	**C**	**λ_{Co} [nm]**	**d_{WC} [nm]**
967	1050	5	0.55	109	202
943	1100	5	0.58	118	205
946	1100	6	0.51	102	205
941	1150	6	0.59	122	205
947	1100	7	0.56	103	200
942	1150	7	0.56	111	187

Figure 4.22 is representing the relation between hardness and compressive strength. The compressive strength has an upward trend with increasing hardness. As shown in the figure, the highest compressive strength and hardness values are approximately 5290 MPa and 1820 HV30 (Sample 967). So that, lower d_{WC}, higher relative density and hardness considerably effect compressive strength. One the one hand it decreases with higher contiguity of WC phase and larger free mean path of Co phase.

It is well known that the strength of ceramics is affected by the specimen size. The ratio of the compressive strength decreases as the specimen size increases. This phenomenon of reduction in strength due to specimen size increase is called the reduction phenomenon and this is due to the fracture mechanics-based derivation of size effect law [79]. Table 4.8 and Figure 4.23 and represents the effect of sample volume on compressive strength.

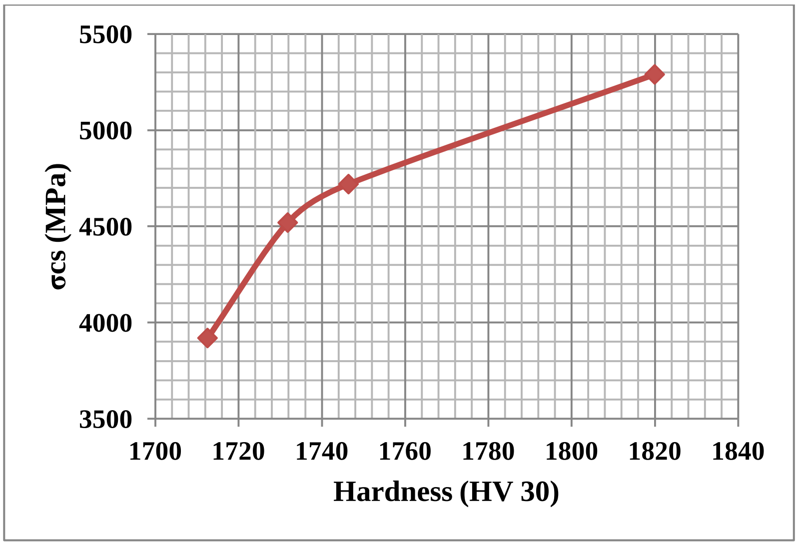

Figure 4.22 Relationship between hardness and compressive strength

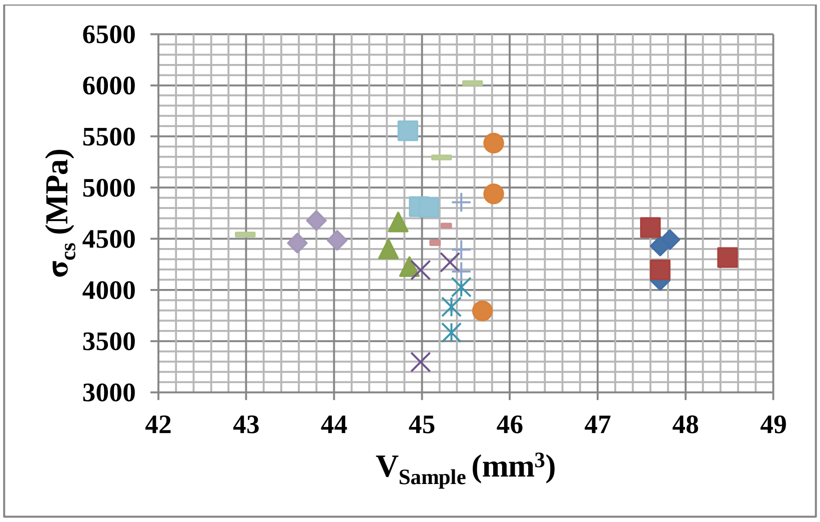

Figure 4.23 Effect of sample volume on compressive strength

As can be seen in the table below, the compressive strength of sample 921, 941 and 975 decreases due to increased specimen volume that are suited to literature reviews. Although the sample volume increases, the compressive strength of other samples increases, too. The reasons for this deviation are inhomogenities, surface qualities of samples and density differeneces.

Table 4.8 The volume and compressive strength values of the samples, respectively

Sample	**Volume [mm^3]**	**Compressive Strength [MPa]**
919	47.82, 47.71, 47.71	4489.68, 4427.57, 4092.20
921	47.71, 47.60, 48.48	4195.06, 4608.02,4314.71
941	44.62, 44.86, 44.73	4398.69, 4226.45, 4662.70
942	45.32, 44.99, 44.99	4268.5, 4192.32, 3293.26
943	45.45, 44.34, 44.34	4026, 3581.15, 3832.80
946	45.7, 45.82, 45.82	3793.36, 4936.89, 5433.31
947	45.45, 45.45, 45.45	4855.16, 4178.01, 4391.97
966	45.23, 45.1, 45.1	4626.68, 4461.97, 4455.97
967	45.58, 45.22, 43.0	6019.30, 5293.22, 4593.06
974	43.58, 43.80, 44.04	4456.39, 4676.48, 4483.23
975	44.84, 44.97, 45.08	5553.90, 4812.56,4805.30

Table 4.9 shows the values of dynamic compressive strength. The reason of higher value of dynamic compressive strength than quasistatic compressive strength is energy dissipation due to simultaneously growth of several cracks.

Table 4.9 Dynamic compressive strength of samples

Sample Number	**$t_{Milling}$ (min)**	**T_{Sinter} [^{o}C]**	**t_{Sinter} [min]**	**$\dot{T}_{Cool}$ [K/min]**	**$\sigma_{cs,dynamic}$ [MPa]**	**$\sigma_{cs,quasistatic}$ [MPa]**
966	1000	1150	5	100	4630±40	4520±80
967	1000	1050	5	100	4640±415	5290±605
974	1000	1050	5	200	4960±340	4540±100
975	1000	1050	5	150	4670±310	5060±350

The amount of samples and surface quality can cause deviations from the expected results. Table 4.10 shows the result of SHPB experiment due to 2 wave analysis.

Table 4.10 SHPB result of sample 974

Sample Number	$t_{Milling}$ [min]	T_{Sinter} [°C]	t_{Sinter} [min]	$\dot{T}_{Cool}$ [K/min]	$\sigma_{cs,\ quasistatic}$ [MPa]	$\sigma_{cs,DWT}$ [MPa]	$\sigma_{cs,\ SHBP}$ [MPa]
974	1000	1050	5	200	4540±100	4960±340	5670±127

The compressive strength was determined at the different strain rate via the quasitatic, drop weight and SHPB tests (Figure 4.24). So that, the strain hardening exponent (N) can be determined due to the compressive strength-strain rate curve. The slope of log compressive strength-strain rate curve equals to value of N (Figure 4.25).

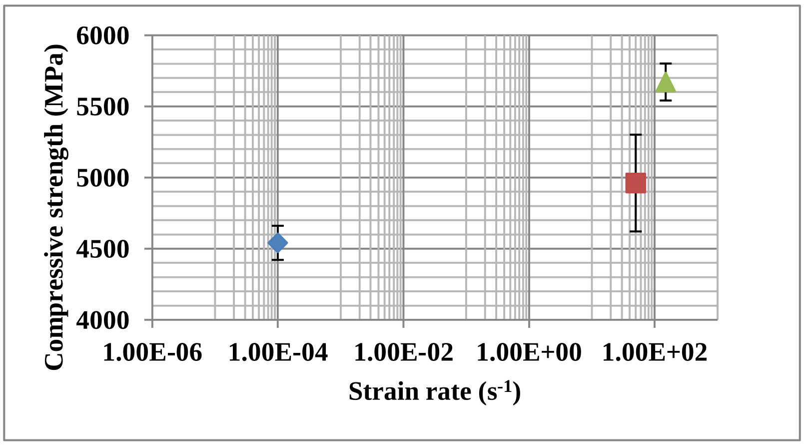

Figure 4.24 The strain rate and compressive strength of sample 974

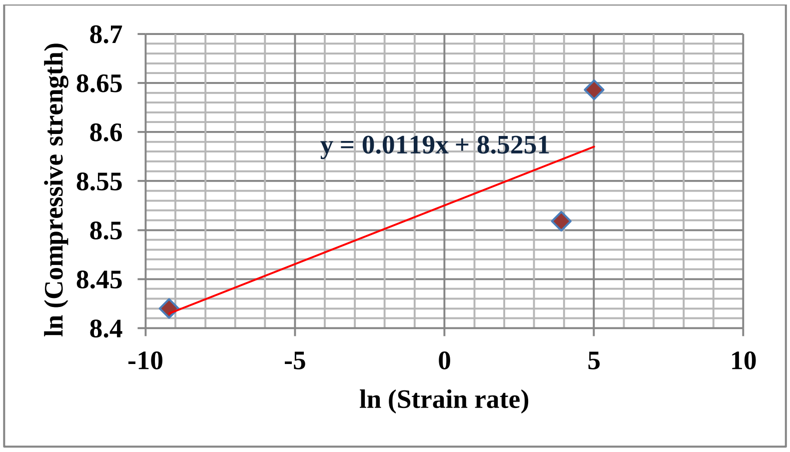

Figure 4.25 The natural log of the compressive strength versus the natural log of the strain rate for sample 974

According to Figure 4.25 the N value is 0.0119. N ranging from $5 \cdot 10^{-3}$ to $20 \cdot 10^{-3}$ for brittle materials [80].

4.3.3 Elastic modulus

Table 4.11 includes values of elastic modulus according to experimental results.

Table 4.11 Elastic modulus of samples due to ultrasonic test method

Sample No	$t_{Milling}$ [min]	T_{Sinter}[°C]	t_{Sinter}[min]	$\dot{T}_C$ [K/min]	E [GPa]
895	500	1150	5	93.3	557
919	1000	1150	5	93.3	549
921	1500	1150	5	93.3	544
941	1000	1150	6	100	556
942	1000	1150	7	100	554
943	1000	1100	5	100	553
946	1000	1100	6	100	556
947	1000	1100	7	100	572
966	1000	1150	5	100	566
967	1000	1050	5	100	558
974	1000	1050	5	200	554
975	1000	1050	5	150	553

The elastic modulus depends on the density of material. During the ultrasonic measurement pores lead to a disturbing acoustic noise level. So that relative density of samples effects the results. The small height of samples (approximately 4 mm) can cause deviations at the determination of elastic modulus. According to EN 843-2, the height of samples should be at least 5mm in the measuring direction [75].

Figure 4.26 shows the effect of relavite density on elastic modulus. As can be seen in the figure below, higher elastic modulus values were determined due to higher relative density. As a result of low porosity increases stiffness of materials. The elastic modulus and relative density values of the samples 966, 941 and 942 are 566 GPa, 99.3 %, 556 GPa, 99.2 % and 554 GPa, 98.9 % respectively. So that the elastic modulus of the sample 942 is lower than the other samples.

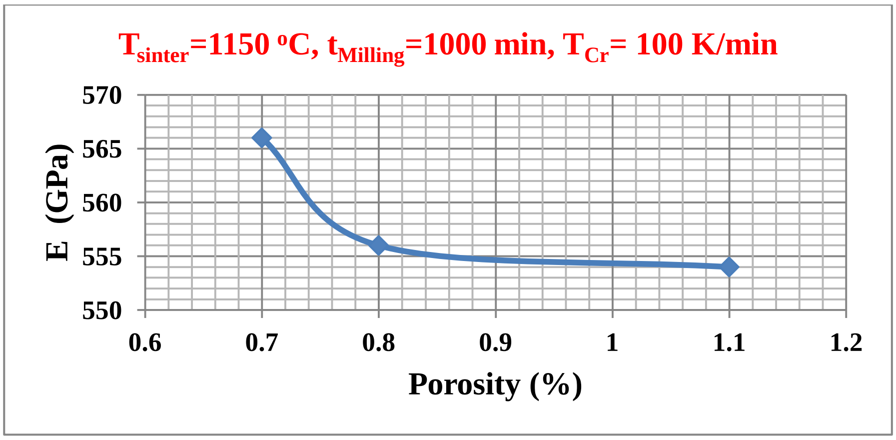

Figure 4.26 Elastic modulus and relative density

Figure 4.27 illustrates the influence of d_{WC} on elastic modulus. As a result of grain growth, the value of elastic modulus decreases regardless of sintering time and sintering temperature. As stated previously the effect of sintering temperature and time on the grain size of d_{WC} is not significant. Hardness is dependent on elastic modulus. When the elastic modulus increases hardness increases due to increasing stiffness. This relation is significant betwen the sample 941 and 942 (Figure 4.28).

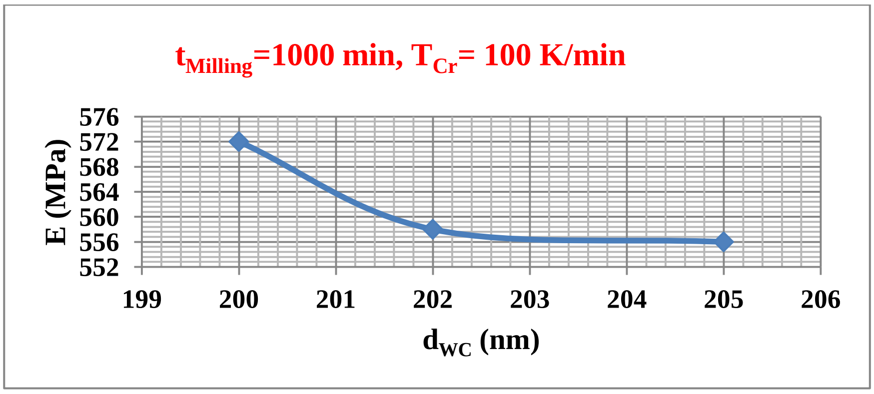

Figure 4.27 Correlation between grain size of WC phase and elastic modulus

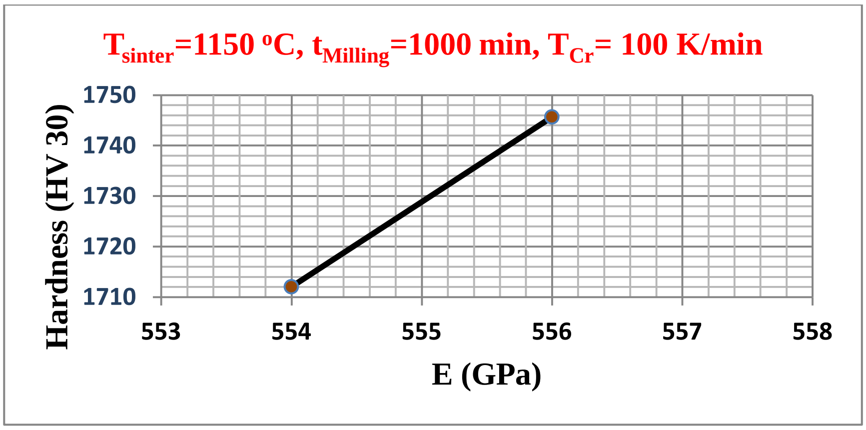

Figure 4.28 Elastic modulus and hardness

Higher cooling rates have an effect on grain size and a lower grain size was observed due to higher cooling rate. But this effect was not significant and lower hardness values were not determined with higher grain size. So that higher hardness and elastic modulus values were determined at low cooling rates due to higher relative density (Figure 4.29). Also internal stresses could increase with increasing cooling rate and this can affect the elastic modulus, too.

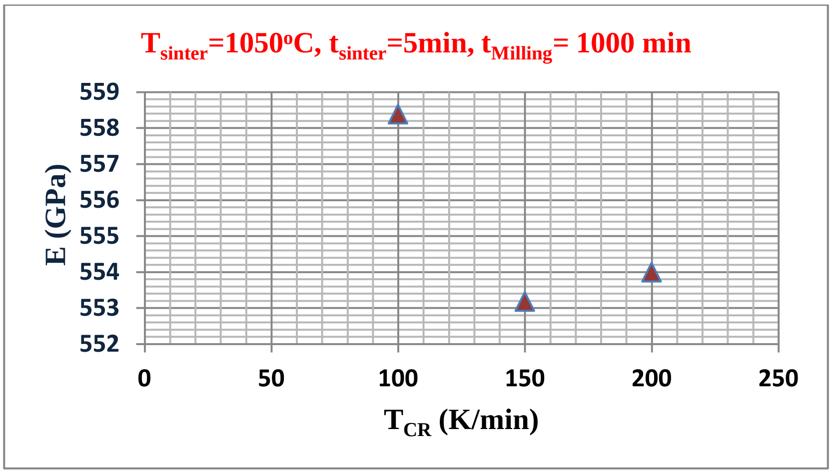

Figure 4.29 Cooling rate and elastic modulus

CHAPTER 5

OUTLOOK

In this thesis, the milling and sintering behaviour of self-mixed WC-12Co powders was investigated. Microstructure and mechanical characteristics of the spark plasma sintered WC-Co hard materials were determined and discussed. The failure behaviour of the produced SPS materials was investigated as a function of the loading rate.

For the preparation of the WC-12Co powder, WC powder from “H.C. Stark” and Co powder from “Umicore” were used. Milling time was varied between 500-1500 min at 130 rpm to prepare a powder charge of 45 g WC-12Co. In different samples, the influence of milling time and sintering conditions on the mechanical properties (hardness, fracture toughness, static and dynamic compressive strength and elastic modulus) was investigated.

The result of increased milling time, the reduction of the powder particle size was determined. On the one hand homogeneous Co distribution or a significant influence on the properties of sintered samples was not observed. Also, the specific area was increased due to decreasing of grain size. Therefore much more energy is required to activation of new surface area.

Sintering temperature and time was varied between 1050-1150^{o}C and 5-7 min, respectively to observe changing of relative density due to sintering conditions. The influence of sintering time and sintering temperature on the WC grain size is insignificant. However contiguity of WC phase and mean free path of Co phase increases with increasing sintering temperature. Cooling rates of 100 K/min, 150 K/min and 200 K/min were applied, respectively. Although grain growth was occured by slow cooling, the reduction of hardness was not observed due to higher relative density values.

The scanning electron micrographs of the WC-Co samples illustrate that Co accumulations appear mostly perpendicular to the direction of applied force and this results in a difference of mechanical properties and there is only a small difference in the structural composition of the samples in radial direction. Porosity can take place as a result of Co flowing. On the one hand, there is also the possibility that Co can diffuse the graphite foil during the sintering process. According to SEM images of the samples, the η-phase fraction is not detected.

The hardness values of WC-12Co samples were between 1610 and 1820 HV30. This shows a large dependency on the relative density (98.9 % - 99.3 %). Furthermore, the fracture toughness of the sample was obtained 9.9-10.6 MPa√m. An increased fracture toughness was achieved by controlled cooling from the sintering temperature.

The quasi-static compressive strength values deviate between 3820-5290 MPa and the dynamic compressive strength values are higher due to inertial effects and dynamic crack propagation. The elastic modulus of the samples were obtained between 544.6 and 572 GPa via the ultrasonic method. The determined values of elastic modulus are dependent on relative density and WC grain size.

REFERENCES

1] Kim, C.S., (2006). Microstructural-Mechanical Property Relationship in WC-Co Composites, Ph. D. Thesis, Materials Science and Engineering Departmant, Carnegie Mellon University, Pittsburgh.

[2] Nishizawa, T. and Ishida, K., (1983). “The Cobalt System”, Bulletin of Phase Diagrams, 4 (4): 387.

[3] Upadhyaya, G.S., (2001). “Materials Science of Cemented Carbides-An Overview”, Materials and Design, 22: 483-489.

[4] Upadhyaya, G.S., (1998). Cemented Tungsten Carbides, Noyes Publications, New Jersey.

[5] Sommer, M., Schubert W.-D., Zobetz E. and Warbichler P., (2002). “On the Formation of very Large WC Crystals During Sintering of Ultra Fine WC-Co Alloys”, International Journal of Refractory Metals and Hard Materials, 20: 41-50.

[6] Kim, S., Han, S.-H., Park, J.-K. and Kim, H.-E., (2003). “Variation of WC Grain Shape with Carbon Content in the WC-Co Alloys During Liquid-Phase Sintering”, Scripta Materialia, 48: 635-639.

[7] ISO 4499-2, (2008). Metallographic determination of Microstructure-Part 2: Measurement of WC Grain Size, ISO, Switzerland.

[8] Jia, K., Fischer, T.E. and Gallois, B., (1998). “Microstructure, Hardness and Toughness of Nanostructured and Convenional WC-Co Composites”, Nano Structured Materials, 10 (5): 875-891.

[9] Radajewski, M., (2011). Herstellung und mechanisches Werkstoffverhalten von WC-Co-Hartmetallen durch SPS, Diplomarbeit, Fakultaet für Werkstoffwissenschaft und Werkstofftechnologie, TU Bergakademia Freiberg, Freiberg.

[10] Bonache, V., Salvador, M.D., Amigo, V. and Busquets, D., (2010). “Spark Plasma Sintering of Nanocrystalline WC-12Co Cermets”, Ceramic Transactions, 209: 367-378.

[11] Hulbert, D.M., Anders, A., Dudina, D.V. and Andersson, J., (2008). “The Absence of Plasma in Spark Plasma Sintering”, Journal of Applied Physics, 104 (3).

[12] Raethel, J., Herrmann, M. and Beckert, W., (2009).“Temperature Distribution for Electrically Conductive and Non-Conductive Materials During Field

Assisted Sintering (FAST)", Journal of the European Ceramic Society, 29: 1419-1425.

[13] Schubert, W.D., Bock, A. and Lux, B., (1995). "General Aspects and Limits of Conventional Ultrafine WC Powder Manufacture and Hard Metal Production", International Journal of Refractory Metals and Hard Materials, 13: 281-296.

[14] Lavergne, O., Robaut, F., Hodaj, F. and Allibert, C.H., (2002). "Mechanism of Solid-State Dissolution of WC in Co-Based Solutions", Acta Materialia, 50: 1683-1692.

[15] Garay, J.E., (2010). "Current-Activated, Pressure-Assisted Densification of Materials", Annual Review of Materials Research, 40: 445-468.

[16] Fang, Z.Z., Wang, X., Ryu, T. and Hwang, K.S., (2009). "Synthesis, Sintering, and Mechanical Properties of Nanocrystalline Cemented Tungsten Carbide", Int. Journal of Refractory Metals and Hard Materials, 27: 288-299.

[17] Ou, X.Q., Song, M., Shen, T.T. and Xiao, D.H., (2011). "Fabrication and Mechanical Properties of Ultrafine Grained WC-10Co-0,45Cr_3C_2-0,25VC Alloys", Int. Journal of Refractory Metals and Hard Materials, 29: 260-267.

[18] Bonache, V., Salvador, M., Fernandez and D.A. Borrelland, A., (2010). "Fabrication of Full Density Near-Nanostructured Cemented Carbides by Combination of VC/Cr_3C_2 Addition and Consolidation by SPS and HIP Technologies", Int. Journal of Refractory Metals and Hard Materials, 29 (2): 202-208.

[19] Sun, L., Yang, T., Jia, C. and Xiong, J., (2011). "VC, Cr_3C_2 Doped Ultrafine WC-Co Cemented Carbides Prepared by Spark Plasma Sintering", Int. Journal of Refractory Metals and Hard Materials, 29 (2): 147-152.

[20] Munir, Z.A., Anselmi-Tamburini, U. and Ohyanagi, M., (2006). "The Effect of Electric Field and Pressure on the Synthesis and Consolidation of Materials: A Review of the Spark Plasma Sintering Method", Journal of Materials Science, 41 (3): 763-777.

[21] Vanmeensel, K., Laptev, A., Hennicke, J. and Vleugels, J., (2005). "Modelling of the Temperature Distribution During Field Assisted Aintering", Acta Materialia, 53: 4379-4388.

[22] Munos, S. and Anselmi-Tamburini, U., (2010). "Temperature and Stress Fields Evolution During Spark Plasma Sintering Processes", Journal of Materials Science, 45 (23): 6528-6539.

[23] Anselmi-Tamburinia, U., Gennari, S., Garay, J.E. and Munir, Z.A., (2005). "Fundamental Investigations on the Spark Plasma Sintering/Synthesis Process II. Modeling of Current and Temperature Distributions", Materials Science and Engineering A, 394: 139-148.

[24] Langer, J., Quach, V., Groza, J.R. and Guillon, O., (2010). "A Comparison Between FAST and SPS Apparatuses Based on the Sintering of Oxide Ceramics", Int. Journal of Applied Ceramic Technology, 1-9.

[25] Cha, S.I., Hong, S.H. and Kim, B.K., (2003). "Spark Plasma Sintering Behavior of Nanocrystalline WC-10Co Cemented Carbide Powders", Materials Science and Engineering A, 351: 31-38.

[26] FCT Systeme GmbH Raunenstein/D, Publications and Press, http://www.fct-systeme.de/en/content/Download_News_Presse/~nm.67~nc.69/Publications-and-Press.html, 27 September 2011.

[27] Munir, Z.A., Quach, D.V. and Ohyanagi, M., (2011). “Electric Current Activation of Sintering: A Review of the Pulsed Electric Current Sintering Process”, Journal of the American Ceramic Society, 94 (1): 1-19.

[28] Kim, H.-C., Shon, I.-J., Yoon, J.-K. and Doh, J.-M., (2007). “Consolidation of Ultra Fine WC and WC-Co Hard Materials by Pulsed Current Activated Sintering and Its Mechanical Properties”, Int. Journal of Refractory Metals and Hard Materials, 25: 46-52.

[29] Zhao, S., Song, X., Wei, C. and Zhang, L., (2009). “Effects of WC Particle Size on Densification and Properties of Spark Plasma Sintered WC-Co Cermet”, Int. Journal of Refractory Metals and Hard Materials, 27: 1014-1018.

[30] Gille, G., Bredthauer, J., Gries, B., Mende, B. and Heinrich, W., (2000). “Advanced and New Grades of WC and Binder Powder - Their Properties and Application”, Int. Journal of Refractory Metals and Hard Materials, 18: 87-102.

[31] Lee, H.C. and Gurland, J., (1978). “Hardness and Deformation of Cemented Tungsten Carbide”, Materials Science and Engineering, 33: 125-133.

[32] Xu, Z.-H. and Agren J., (2004). “A Modified Hardness Model for WC-Co Cemented Carbides”, Materials Science and Engineering A, 386: 262-268.

[33] Cha, S.I., Lee, K.H., Ryu, H.J. and Hong, S.H., (2008). “Analytical Modeling to Calculate the Hardness of Ultra-Fine WC-Co Cemented Carbides”, Materials Science and Engineering A, 489: 234-244.

[34] Chermant, J.L. and Osterstock, F., (1976). “Fracture Toughness and Fracture of WC-Co Composites”, Journal of Materials Science, 11 (10): 1939-1951.

[35] Schubert, W.D., Neumeister, H., Kinger, G. and Lux, B., (1998). “Hardness to Toughness Relationship of Fine-Grained WC-Co Hardmetals”, International Journal of Refractory Metals and Hard Materials, 16 (2): 133-142.

[36] Shetty, D.K., Wright, I.G., Mincer, P.N. and Clauer, A.H., (1985). “Indentation Fracture of WC-Co Cermets”, Journal of Materials Science, 20: 1873-1882.

[37] Roebuck, B. and Coles, W., (1992). “Mechanical Test Discriminability for WC Hardmetals”, Refractory Metals and Hard Materials, 11: 127-136.

[38] Spiegler, R., Schmauder, S. and Sigl, L.S., (1990). “Fracture Toughness Evaluation of WC-Co Alloys by Indentation Testing”, Journal of Hard Materials, 1 (3): 147-158.

[39] Niihara, K., Morena, R. and Hasselman, D.P.H., (1982). “Evaluation of K_{Ic} of Brittle Solids by the Indentation Method with Low Crack-to-Indent Ratios”, Journal of Materials Science Letters, 1 (1): 13-16.

[40] Torres, Y., Casellas, D., Anglada and M., Llanes, L., (2001). “Fracture Toughness Evaluation of Hardmetals: Influence of Testing Procedure”, International Journal of Refractory Metals and Hard Materials, 19: 27-34.

[41] Ferreira, J.A.M., Pina Amaral, M.A., Antunes, F.V. and Costa, J.D.M., (2009). “A Study on the Mechanical Behaviour of WC/Co Hardmetals”, Int. Journal of Refractory Metals and Hard Materials, 27: 1-8.

[42] Klünsner, T. and Marsoner, S., (2010). “Effect of Microstructure on Fatigue Properties of WC-Co Hard Metals”, Procedia Engineering, 2 (1): 2001-2010.

[43] Sailer, T., Herr and M., (2001). “Microstructure and Mechanical Properties of Ultra Fine-Grained Hardmetals”, Int. Journal of Refractory Metals and Hard Materials, 19: 553-559.

[44] Okamoto, S. and Nakazono, Y., (2005). “Mechanical Properties of WC/Co Cemented Carbide with Larger WC grain Size”, Materials Characterization, 55: 281-287.

[45] Wang, H. and Remesh, K.T., (2004). “Dynamic Strength and Fragmentation of Hot-Pressed Silicon Carbide Under Uniaxial Compression”, Acta Materialia, 52: 355-367.

[46] Kraft, R.H., Molinari, J.F., Ramesh, K.T. and Warner, D.H., (2008). “Computational Micromechanics of Dynamic Compressive Loading of A Brittle Polycrystalline Material Using A Distribution of Grain Boundary Properties”, Journal of the Mechanics and Physics of Solids, 56: 2618-2641.

[47] Nemat-Nasser, S. and Deng, H., (1994). “Strain-Rate effect on Brittle Failure in Compression”, Acta Metallurgica Et Materialia, 42, (3): 1013-1024.

[48] Golovchan, V.T. and Litoshenko, N.V., (2010). “The Stress-Strain Behavior of WC-Co Hardmetals”, Computational Materials Science, 49: 593-597.

[49] Doi, H., Fujiwara, Y., Miyake, K. and Oosawa, Y., (1970). “A Systematic Investigation of Elastic Moduli of WC-Co Alloys”, Metallurgical and Materials Transactions, 1(5): 1417-1425.

[50] Ivensen, V.A., Eiduk, O.N. and Chistyakova, V.A., (1974). “Dependence of the Yield Strength of WC-Co Hard Alloys on Their Cobalt Content and Tungsten Carbide Grain Size”, Powder Metallurgy and Metal Ceramics, 13, (5): 413-415.

[51] Zhang, H., Lu, Q., Zhang, L. and Fang, Z.Z., (2010). “Dependence of Microcrack Number Density on Microstructural Parameters During Plastic Deformation of WC-Co Composite”, Int. Journal of Refractory Metals and Hard Materials, 28 (3): 434-440.

[52] Chernyavskii, K.S., Travushkin, G.G., Sapronova Z.N. and Aleksandrovieh, A.A., (1991). “Micromechanism of Deformation and Failure at Successive Stages of Compressive Loading of Hard Alloys WC-Co”, Strength of Materials, 25 (10): 746-754.

[53] Jayaram, V., Sinclair, R. and Rowcliffe, D.J., (1983). “Intergranular Cracking in WC-6Co: An Application of the von Mises Criterion”, Acta Metallurgica, 31 (3): 373-378.

[54] Sarin, K. and Johannesson, T., (1975). “On the Deformation od WC-Co Cemented Carbides”, Metal Science, 9 (10): 472-476.

[55] Rettenmayr, M., Exner, H.E. and Mader, W., (1988). “Electron Microscopy of Binder Phase Deformation in WC-Co Alloys”, Materials Science and Technology, 4: 984-990.

[56] Sigl, L.S. and Exner, H.E., (1987). “Experimental Study of the Mechanics of Fracture in WC-Co Alloys”, Metallurgical Transactions. A, Physical Metallurgy and Materials Science, 18 A (7): 1299-1308.

[57] Fischmeister, H.F., Schmauder, S. and Sigl, L.S., (1988). “Finite Element Modelling of Crack Propagation in WC-Co Hard Metals”, Materials Science and Engineering, 105 (2): 305-311.

[58] Sigl, L.S., Mataga, P.A., Dalgleish, B.J. and McMeeking, R.M., (1988). “On the Toughness of Brittle Materials Reinforced with A Ductile Phase”, Acta Metallurgica, 36 (4): 945-953.

[59] Ritchie, R.O., (1988). “Mechanisms of Fatigue Crack Propagation in Metals, Ceramics and Composites: Role of Crack Tip Shielding”, Materials Science and Engineering A, 103 (1): 15-28.

[60] Richter, V. and Ruthendorf, M.V., (1999). “On Hardness and Toughness of Ultra Fine and Nanocrystalline Hard Materials”, Int. Journal of Refractory Metals and Hard Materials, 17 (1-3): 141-152.

[61] Sherif El-Eskandaranya, M., Mahdaya Amir, A., Ahmedb, H.A. and Amera A.H., (2000). “Synthesis and Characterizations of Ball-Milled Nanocrystalline WC and Nanocomposite WC–Co Powders and Subsequent Consolidations”, Journal of Alloys and Compounds, 312: 315–325.

[62] All about Cemented Carbide, Cemented Carbide, http://www.allaboutcementedcarbide.com/01_05.html, 30 September 2011.

[63] German, R.M., (2005). Metall Powder Metallurgy and Particulate Materials Processing, Metal Powder Industry.

[64] ISO 9277, (2010). Determination of the Specific Surface Area of Solids by Gas Adsorption Using the BET Method, ISO, Switzerland.

[65] Brunauer, S., Emmett, P.H. and Teller E., (1938). “Adsorption of Gases in Multimolecular Layers”, Journal of the American Chemical Society, 60 (2): 309-319.

[66] Jiquio, L. and Baiyun, H., (2001). “Particle Size Characterization of Ultrafine Tungsten Powder”, International Journal of Refractory Metals and Hard Materials, 19: 89-99.

[67] Pfeifer, P. and Avnir, D., (2001). “Chemistry in Noninteger Dimensions Between Two and Three. I. Fractal Theory of Heterogeneous Surfaces”, Journal Physics and Chemistry, 79 (7): 89-99.

[68] ISO 3369, (2006). Impermeable Sintered Metal Materials and Hardmetals Determination of Density, ISO, Switzerland.

[69] Echlin, P., (2009). Handbook of Sample Preparation for Scanning Electron Microscopy and X-Ray Microanalysis, Springer, New York.

[70] ISO 3878, (1983), Hardmetals-Vickers Hardness Test, ISO, Switzerland.

[71] ISO 6507-1, (2005), Metallic Materials-Vickers Hardness Test-Part 1: Test Method, ISO, Switzerland

[72] ISO 4506, (1979), Hardmetals-Compression Test, ISO, Switzerland

[73] ASM Handbook Comitee, (2000), Mechanical Testing and Evaluation, Volume 8, Northeast Ohio.

[74] Chen, W. and Song, B., (2011). “Split Hopkinson (Kolsky) Bar Design, Testing and Applications”, Springer, New York.

[75] EN 843-2, (2006), Advanced Technical Ceramics-Mechanical Properties Of Monolithic Ceramics At Room Temperature-Part 2: Determination Of Young's Modulus, Shear Modulus And Poisson's Ratio, CEN, Brussels.

[76] Bonache, V., Rayon, E., Salvador, M.D. and Busquets D., (2010). “Nanoindentation Study of WC-12Co Hardmetals Obtained From Nanocrystalline Powders: Evaluation of Hardness and Modulus on Individual Phases”, Materials Science and Engineering A, 527 (12): 2935-2941.

[77] Suetin, D.V., Shein, I.R. and Ivanovskii, A.L., (2009). “Structural, Electronic and Magnetic Properties of η Carbides (Fe_3W_3C, Fe_6W_6C, Co_3W_3C and Co_6W_6C) From First Principles Calculations”, Physica B: Condensed Matter, 404 (20): 3544-3549.

[78] Sun, L., Jia, C.-C. and Xian, M., (2007). “A Research on the Grain Growth of WC-Co Cemented Carbide”, Int. Journal of Refractory Metals and Hard Materials, 25 (2): 121-124.

[79] Bazant, P.Z., Fellow, A. and Xiang, Y., (1997). “Size Effect in Compression Fracture: Splitting Crack Band Propagation”, Journal of Engineering Mechanics, 12232.

[80] Henschel, S., (2011). SPS-Synthese und Charakterisierung des mechanischen Werkstoffverhaltens von Volumenhartstoffen aus dem System Ti-Al-N, Diplomarbeit, Fakultaet für Werkstoffwissenschaft und Werkstofftechnologie, TU Bergakademia Freiberg, Freiberg.

CURRICULUM VITAE

PERSONAL DETAILS

Name and Surname : Alihan AYGUN

Date and Place of Birth : 13.05.1987-Trabzon

Foreign Language : English, German

E-mail : alihan_aygun@hotmail.com

EDUCATION

Degree	Department	School/University	Graduation Year
Master	Material Science Engineering	Yıldız Technical University TU BA Freiberg (ERASMUS)	2012
Bachelor	Chemical Engineering	Yıldız Technical University	2011
	Metallurgical and Materials Engineering	Yıldız Technical University	2010
High School	-	Mensucat Santral Anatolian High School	2005

WORK EXPERIENCE

Year	Company/Corporation	Enrollment
2013	ERDEMIR T.A.S	Quality Engineer

2010	Burak Aluminium Inc.	Trainee (20 weekdays)
2009	Erdemir Trade Inc.	Trainee (30 weekdays)
2008	Kardemir Inc.	Trainee (30 weekdays)